International Journal of Mechanical Sciences 117 (2016) 53–66

Contents lists available at ScienceDirect

International Journal of Mechanical Sciences

journal homepage: www.elsevier.com/locate/ijmecsci

The effect of yield surface curvature change by cross hardening on forming limit diagrams of sheets

C. Soyarslan [a,*], B. Klusemann [b,c], S. Bargmann [a,c]

[a] Institute of Continuum Mechanics and Material Mechanics, Hamburg University of Technology, Hamburg, Germany
[b] Institute of Product and Process Innovation, Leuphana University of Lüneburg, Lüneburg, Germany
[c] Institute of Materials Research, Helmholtz-Zentrum Geesthacht, Geesthacht, Germany

ARTICLE INFO

Article history:
Received 22 December 2015
Received in revised form
20 June 2016
Accepted 22 July 2016
Available online 3 August 2016

Keywords:
Forming limit diagram
Plasticity
Anisotropy
Sheet metal forming
Cross hardening
Nakazima test
Marciniak-Kuczyński test

ABSTRACT

The paper aims at clarification of the role of reduction in yield locus curvature on forming limit diagrams. To this end, a cross-hardening model showing a reduction of yield surface curvature is used which accounts for dynamic and latent hardening effects associated with dislocation motion during loading. The model's three-dimensional tensorial as well as reduced plane-stress vector formulations are given. The first quadrants of forming limit diagrams are numerically produced using finite element models of the Marciniak-Kuczyński test with spatially correlated random defect distribution as localization triggering mechanism. The effect of cross hardening is investigated in detail. It is demonstrated that for plane strain loading path there occurs no difference in localization predictions of the models with and without cross hardening whereas for biaxial strain paths a delayed localization is observed in the cross hardening model as compared to the one without cross hardening effects. This is in accordance with the relative bluntness of the yield surface at the points of load path change towards localization. These results are complemented by Nakazima test simulations where similar observations are made.

1. Introduction

Process design for functional yet lightweight components requires an accurate description of the material behavior during deformation in order to fully exploit the potential of materials and processes. The finite-element-based modeling has proven to be an efficient way to predict the material and structural behavior and is nowadays standard in industrial practice. However, the applicability and benefits of simulation strongly depends on the accuracy of the underlying constitutive material model. With regard to complex forming simulations, the efficient modeling of sheet metals is of special interest. There exists a number of phenomenological models, e.g., accounting for isotropic and kinematic hardening, which accurately describe the material behavior of sheet metals under uniaxial deformation conditions. However, as stated by Wagoner et al. [38], the deformation in real forming processes involves a number of strain path changes requiring special attention which is more complex than a uniaxial strain or stress state. Therefore more complicated models are required to accurately model the loading-path dependent behavior of sheet metals in forming simulations. In this regard, the present or emergent underlying microstructure plays a crucial role. Physical based models are developed accounting for microstructural changes during complex deformation states, in particular orthogonal loading-path changes [36,22,32]. These, still phenomenological models, are often based on the evolution and distortion of one or two yield surfaces [2,21]. A particular class of material models, interesting for this work, model the loading path dependent microstructure changes with one yield surface determined by an evolving anisotropy tensor [7,22,6,31,4,3,5].

Of particular interest for the design and optimization of forming processes is the formability limit.[1] Following the definition of Banabic [1], the formability describes the capability of a material to undergo plastic deformation to a given shape without defects. The probably mostly used theory is based on the early work by Marciniak and Kuczyński [24], where on basis of a geometrical inhomogeneity (e.g., thickness variation in a distinct region), the onset of strain localization, representing the initiation point of failure or necking, is obtained. The model by Marciniak and Kuczyński has been widely applied as well as modified to improve its applicability [13,29,17,8,18,19,23]. In addition to process parameters, formability inevitably depends on the

* Corresponding author.
E-mail address: celal.soyarslan@tu-harburg.de (C. Soyarslan).

[1] Different types of forming limit diagrams exist, depending on the stress procedure [16,24,10,29] and on the measure of limiting strain measures, e.g., necking or fracture.

http://dx.doi.org/10.1016/j.ijmecsci.2016.07.028

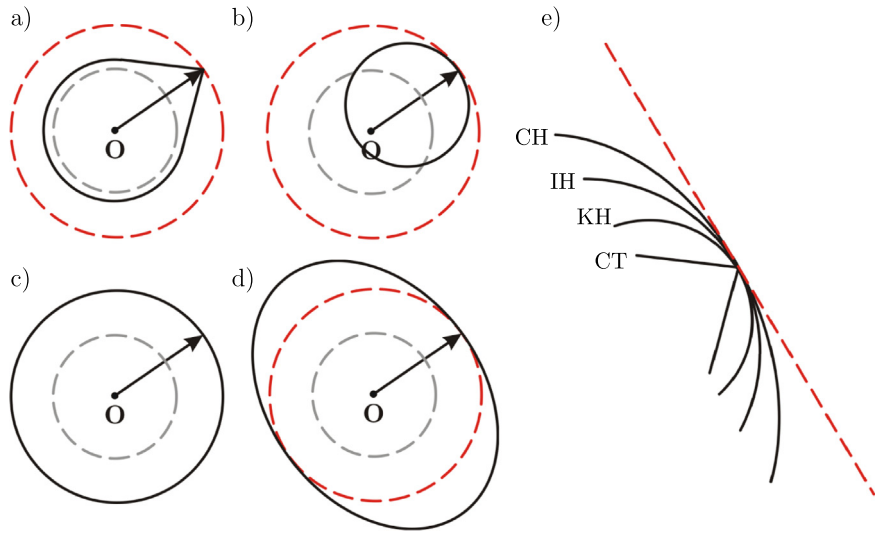

Fig. 1. A schematic depiction of yield locus evolution with different continuum theories: a) corner theory (CT), b) kinematic hardening (KH), c) isotropic hardening (IH), d) cross hardening (CH). e) closer look at the yield locus curvature at the point of loading. The red dashed line represents the limit $\rho \to \infty$ where ρ is the radius of curvature. As seen from corner theories to cross hardening the yield locus curvature systematically decreases. Gray dashed lines: initial yield loci. Red dashed lines: reference isotropic hardening yield loci. (For interpretation of the references to color in this figure legend, the reader is referred to the web version of this article.)

material properties. For instance, in associative plasticity yield locus curvature affects the formability limits of the material. The over-stiffness of the associative J_2 plasticity theory in prediction of plastic instabilities under distinctly nonproportional stress histories is well known [37]. Tvergaard [37] shows that a better agreement with the experimental necking strains is obtained using pure kinematic hardening in which the yield surface curvature remains constant. The reason is linked to the yield surface curvature, which is reduced in isotropic hardening. In crystal plasticity the overall yield surface forms as an envelope of individual glide yield surfaces. Vertices and corners then naturally arise at the loading point due to sliding on favorably oriented glide planes. Unlike smooth yield theories, where a tangential component of the stress loading $\mathrm{d}\boldsymbol{\sigma}_{\mathrm{tangent}}$ does not cause a plastic flow, plastic flow occurs in vertex theories. For a given finite, nonproportional stress change, more strain change occurs for a yield surface with high curvature at the loading point than that occurs for the yield surface with lower curvature. A demonstration of the yield loci evolution for various plastic hardening models are given in Fig. 1.

As illustrated in Fig. 2, cross hardening results in reduced yield locus curvature. This macroscopic response of the polycrystal is physically linked to the evolution of dislocation microstructure during plastic deformation [22]. For IF (interstitial free) steels, e.g., DC06, a cellular structure is formed by dislocations accumulating at cell boundaries under monotonic loading paths. In subsequent orthogonal paths, these dislocations structures act as obstacles for newly activated slip systems resulting in latent resistance to yielding and the hardening rate increase is named as cross hardening [5]. Contrary to Tvergaard's observations, which suggests a requirement for yield locus curvature increase in order to meet experimental necking strains, Levkovitch and Svendsen's cross-hardening model [22] signals an additional stiffness over the associative J_2 plasticity theory. Apart from the yield surface curvature, the strain rate sensitivity of the material strongly influences the formability as well. The studies [12,9,13] show that already a small strain-rate sensitivity shift the forming limit to larger strains which lead to better accordance with experiments. Inal et al. [14] employed a rate-sensitive polycrystal plasticity model to obtain FLDs based on the Marciniak-Kuczyński approach. Although the model allows the investigation of the strain-rate sensitivity, this study concentrates on the differences between face-centered-cubic (fcc) and body-centered-cubic (bcc) type slip systems. For fcc type materials a lower forming limit curvature is obtained due to a sharper yield locus compared to bcc type materials. Additionally, it is shown that texture evolution has a negligible effect. The study of Zhang et al. [41] clearly reveals that the formability is increasing for a rate-sensitive material, however, that the forming speed does not influence the material formability for the same rate-sensitive material. In a subsequent study of the same authors [42] two different approaches, one theoretical based on the Marciniak-Kuczyński model and one numerical based on the Marciniak test, are investigated with regard to strain hardening as well as strain rate sensitivity. An increasing formability is observed for an increase of both mechanisms.

With these motivations, in this study we aim to quantify the gained stiffness with the change of the yield surface curvature by investigating the stabilizing effect of the cross hardening on the flow localization predictions, a topic which is not documented in the literature so far. To this end, a reduced plane-stress visco-plastic formulation of Levkovitch-Svendsen's cross-hardening model is developed for thin shells and implemented as a user defined material subroutine into Abaqus. Verification of the code is realized for finite-strain normal and small-strain shear loading scenarios for which analytical derivations are made available (see also [34]). The first quadrant of the forming limit diagram is numerically produced using a two-dimensional finite element model with a spatially correlated random defect distribution in the form of a reduction in yield strength reproducing the classical results by Marciniak and Kuczyński [24] (see also [29]). Additionally, the forming limit capabilities of the material are analyzed based on the Nakazima test [28]. These demonstrate the enhanced formability of the material with decreasing yield locus curvature with cross hardening relative to the classical J_2 flow theory.

2. Theory

2.1. Material model – tensor notation

Considering small deformations, let[2] the total strain tensor $\boldsymbol{\varepsilon} = 1/2\,[\nabla\boldsymbol{u} + (\nabla\boldsymbol{u})^{\mathsf{T}}]$ be additively split into elastic $\boldsymbol{\varepsilon}^e$ and plastic $\boldsymbol{\varepsilon}^p$ parts with $\boldsymbol{u}$ denoting the displacement vector. The stress $\boldsymbol{\sigma}$ is then computed from the stored elastic strain energy density $W = \frac{1}{2}\big[\boldsymbol{\varepsilon} - \boldsymbol{\varepsilon}^p\big]\colon \boldsymbol{C}^e\colon \big[\boldsymbol{\varepsilon} - \boldsymbol{\varepsilon}^p\big]$ viz.

$$\boldsymbol{\sigma} = \frac{\partial W(\boldsymbol{\varepsilon} - \boldsymbol{\varepsilon}^p)}{\partial \boldsymbol{\varepsilon}} = \boldsymbol{C}^e\colon [\boldsymbol{\varepsilon} - \boldsymbol{\varepsilon}^p], \tag{1}$$

where $\boldsymbol{C}^e$ denotes the elastic constitutive tensor with

$$\boldsymbol{C}^e := \frac{\partial^2 W(\boldsymbol{\varepsilon} - \boldsymbol{\varepsilon}^p)}{\partial \boldsymbol{\varepsilon}^2} = K\,\mathbf{1}\otimes\mathbf{1} + 2\mu\,\mathcal{I}^{\mathrm{dev}} = \text{constant}. \tag{2}$$

K represents the bulk modulus whereas μ is the shear modulus. $\mathcal{I}^{\mathrm{dev}}$ is the deviatoric part of the fourth-order symmetric identity tensor, $\mathcal{I}^{\mathrm{sym}} = 1/2\big[\mathbf{1}\,\overline{\otimes}\,\mathbf{1} + \mathbf{1}\,\underline{\otimes}\,\mathbf{1}\big]$, with $\mathcal{I}^{\mathrm{dev}} = \mathcal{I}^{\mathrm{sym}} - 1/3\big[\mathbf{1}\otimes\mathbf{1}\big]$.

The flow stress of the material $\sigma_y\big(e^p, \dot{e}^p\big)$ depends on the equivalent plastic strain e^p and its rate $\dot{e}^p$. The contributions $h_y\big(e^p\big)$ and $r_y\big(\dot{e}^p\big)$ which are respectively associated with strain hardening and strain rate hardening are multiplied to give the total hardening following a Johnson–Cook type formulation [15]:

$$\sigma_y\big(e^p, \dot{e}^p\big) = h_y\big(e^p\big) r_y\big(\dot{e}^p\big). \tag{3}$$

The multiplicative strain $h_y\big(e^p\big)$ and strain rate $r_y\big(\dot{e}^p\big)$ hardening components are defined as

$$\begin{aligned} h_y\big(e^p\big) &:= \sigma_\infty - \big[\sigma_\infty - \sigma_{y0}\big]\exp\big(-m\big[e^p\big]^n\big), \\ r_y\big(\dot{e}^p\big) &:= 1 + c\ \log\big(\dot{e}^p/\dot{e}_0^p\big), \end{aligned} \tag{4}$$

with σ_{y0}, σ_∞, c, n, m and $\dot{e}_0^p$ denoting material parameters. A single-surface elastic domain in the stress space

$$\begin{aligned} \mathbb{E}_\sigma = \{&[\boldsymbol{\sigma}, \boldsymbol{\chi}, \boldsymbol{\mathcal{H}}, e^p, \dot{e}^p] \in \mathbb{S}\times\mathbb{S}\times\mathbb{B}\times\mathbb{R}^+\times\mathbb{R}^+ \\ &: \phi^p(\boldsymbol{\sigma}, \boldsymbol{\chi}, \boldsymbol{\mathcal{H}}, e^p, \dot{e}^p) \le 0\}, \end{aligned} \tag{5}$$

with the flow potential

$$\phi^p(\boldsymbol{\sigma}, \boldsymbol{\chi}, \boldsymbol{\mathcal{H}}, e^p, \dot{e}^p) = \sqrt{[\,\boldsymbol{\sigma} - \boldsymbol{\chi}\,]\colon[\,\boldsymbol{\mathcal{A}} + \boldsymbol{\mathcal{H}}\,]\colon[\,\boldsymbol{\sigma} - \boldsymbol{\chi}\,]} - \sigma_y\big(e^p, \dot{e}^p\big) \tag{6}$$

accounts for combined effects of isotropic, kinematic as well as cross hardening. Here, $\mathbb{S}$ denotes the vector space of symmetric second-order tensors with $\dim(\mathbb{S}) = 6$. Letting $\mathbb{D}$ denote the vector space of symmetric (major and minor) fourth-order tensors and $\dim(\mathbb{D}) = 21$ with $\mathcal{F}_{ijkl} = \mathcal{F}_{jikl} = \mathcal{F}_{ijlk} = \mathcal{F}_{klij}$ for $\mathcal{F}\in\mathbb{D}$, the vector space of symmetric fourth-order tensors which are also deviatoric projections is represented by $\mathbb{B}$ with $\dim(\mathbb{B}) = 15$ with $\mathcal{F}'_{iikl} = 0$ for $\mathcal{F}'\in\mathbb{B}$. While $\boldsymbol{\chi}$ denotes the back-stress controlling the translation of the yield surface, the fourth-order structural tensors (constant) $\boldsymbol{\mathcal{A}}$ and (nonconstant) $\boldsymbol{\mathcal{H}}$ are associated with its initial and evolving form, respectively. The current visco-plastic formulation is referred to as a consistency type visco-plastic formulation, see, e.g., [40], hence during fully developed plastic flow the consistency condition is satisfied, i.e., $\phi^p = 0$.

The plastic flow rule is assumed to be associative and hence it reads

$$\dot{\boldsymbol{\varepsilon}}^p = \dot{e}^p \frac{\partial \phi^p}{\partial \boldsymbol{\sigma}}. \tag{7}$$

The kinematic hardening evolution is modeled with a variant of the Armstrong–Frederick form via

$$\dot{\boldsymbol{\chi}} = c_x\,\dot{e}^p\big[s_x \boldsymbol{n}^p - \boldsymbol{\chi}\big], \tag{8}$$

where c_x and s_x are associated with the saturation rate and magnitude with the back-stress tensor $\boldsymbol{\chi}$. Here, $\boldsymbol{n}^p$ denotes the direction of plastic flow with $\boldsymbol{n}^p = \dot{\boldsymbol{\varepsilon}}^p/|\dot{\boldsymbol{\varepsilon}}^p|$. A generalized plastic work equivalence defines the equivalent plastic strain rate via

$$\dot{e}^p = \frac{\big[\boldsymbol{\sigma} - \boldsymbol{\chi}\big]\colon \dot{\boldsymbol{\varepsilon}}^p}{\sigma_y}. \tag{9}$$

The shape change of the yield surface is controlled by using the projections of $\boldsymbol{\mathcal{H}}$ parallel ($\boldsymbol{\mathcal{H}}^d$) and orthogonal ($\boldsymbol{\mathcal{H}}^l$) to $\boldsymbol{n}^p$ in the rate expression of $\boldsymbol{\mathcal{H}}$ viz.

$$\dot{\boldsymbol{\mathcal{H}}}/\dot{e}^p = c_d\Big[s_d\,\boldsymbol{n}^p\otimes\boldsymbol{n}^p - \boldsymbol{\mathcal{H}}^d\Big] + c_l\Big[s_l\Big[\mathcal{I}^{\mathrm{dev}} - \boldsymbol{n}^p\otimes\boldsymbol{n}^p\Big] - \boldsymbol{\mathcal{H}}^l\Big], \tag{10}$$

where

$$\boldsymbol{\mathcal{H}}^d = \big[\boldsymbol{n}^p\colon\boldsymbol{\mathcal{H}}\colon\boldsymbol{n}^p\big]\big[\boldsymbol{n}^p\otimes\boldsymbol{n}^p\big] \quad\text{and}\quad \boldsymbol{\mathcal{H}}^l = \boldsymbol{\mathcal{H}} - \boldsymbol{\mathcal{H}}^d. \tag{11}$$

The former accounts for growth due to dynamic and the latter due to latent hardening effects. Here, c_d and s_d represent the saturation rate and magnitude associated with $\boldsymbol{\mathcal{H}}^d$, respectively. Analogously, c_l and s_l are the saturation rate and magnitude associated with $\boldsymbol{\mathcal{H}}^l$. For the sake of completeness, Kuhn-Tucker loading/unloading (complementarity) conditions read

$$\dot{e}^p \ge 0,\ \ \phi^p(\boldsymbol{\sigma}, \boldsymbol{\chi}, \boldsymbol{\mathcal{H}}, e^p, \dot{e}^p) \le 0,\ \dot{e}^p\phi^p(\boldsymbol{\sigma}, \boldsymbol{\chi}, \boldsymbol{\mathcal{H}}, e^p, \dot{e}^p) = 0, \tag{12}$$

and the consistency condition is given as

$$\dot{e}^p\dot{\phi}^p(\boldsymbol{\sigma}, \boldsymbol{\chi}, e^p, \dot{e}^p) = 0. \tag{13}$$

3. Reduced plane-stress formulation – vector notation

In this part, we present constrained plane-stress equations in the sense that the plane-stress condition is automatically enforced. To this end, the plane-stress subspace $\hat{\mathbb{S}}\subset\mathbb{S}$ is defined as

$$\hat{\mathbb{S}} := \{\boldsymbol{\sigma}\in\mathbb{S}\colon \sigma_{13} = \sigma_{23} = \sigma_{33} \equiv 0\}, \tag{14}$$

with $\dim(\hat{\mathbb{S}}) = 3$. In addition, we define $\hat{\mathbb{S}}^{\mathrm{dev}}\subset\mathbb{S}$ the subspace of deviatoric symmetric second-order tensors with $\dim(\hat{\mathbb{S}}^{\mathrm{dev}}) = 3$ as

$$\hat{\mathbb{S}}^{\mathrm{dev}} := \{\boldsymbol{\sigma}\in\mathbb{S}\colon \sigma_{13} = \sigma_{23} \equiv 0,\ \mathrm{tr}(\boldsymbol{\sigma}) \equiv 0\}. \tag{15}$$

In reduced plane-stress space implementation, we use 3×1 vectors and 3×3 matrices for the representation of symmetric second-order tensors and fourth-order tensors with at least minor-symmetries. The vector form of the reduced plane-stress space representation of the stress tensor $\hat{\boldsymbol{\sigma}}$ reads $\hat{\boldsymbol{\sigma}} = \Big[\sigma_{11}, \sigma_{22}, \sqrt{2}\sigma_{12}\Big]^{\mathsf{T}}$. The mapping $\widehat{\mathcal{I}}^{\mathrm{dev}}\colon\hat{\mathbb{S}}\to\hat{\mathbb{S}}^{\mathrm{dev}}$ links the stress tensor $\hat{\boldsymbol{\sigma}}\in\hat{\mathbb{S}}$ and its deviator $\mathrm{dev}(\hat{\boldsymbol{\sigma}})\in\hat{\mathbb{S}}^{\mathrm{dev}}$ with $\mathrm{dev}(\hat{\boldsymbol{\sigma}}) = \widehat{\mathcal{I}}^{\mathrm{dev}}\cdot\hat{\boldsymbol{\sigma}}$ where

$$\widehat{\mathcal{I}}^{\mathrm{dev}} = \frac{1}{3}\begin{bmatrix} 2 & -1 & 0 \\ & 2 & 0 \\ \text{sym.} & & 3 \end{bmatrix}. \tag{16}$$

[2] In the rest of the paper, the following notations is used: Consistently assuming $\boldsymbol{a}$, $\boldsymbol{b}$, and $\boldsymbol{c}$ as three second-order tensors, together with the Einstein's summation convention on repeated indices, $\boldsymbol{c} = \boldsymbol{a}\cdot\boldsymbol{b}$ represents the single contraction product with $c_{ik} = a_{ij}b_{jk}$. $d = \boldsymbol{a}\colon\boldsymbol{b} = a_{ij}b_{ij}$ represents the double contraction product, where d is a scalar. $\mathcal{E} = \boldsymbol{a}\otimes\boldsymbol{b}$, $\mathcal{F} = \boldsymbol{a}\,\overline{\otimes}\,\boldsymbol{b}$, and $\mathcal{G} = \boldsymbol{a}\,\underline{\otimes}\,\boldsymbol{b}$ represent the tensor products with $\mathcal{E}_{ijkl} = a_{ij}b_{kl}$, $\mathcal{F}_{ijkl} = a_{ik}b_{jl}$, and $\mathcal{G}_{ijkl} = a_{il}b_{jk}$, where $\mathcal{E}$, $\mathcal{F}$, and $\mathcal{G}$ represent fourth-order tensors. $\boldsymbol{a}^{\mathsf{T}}$ and $\boldsymbol{a}^{-1}$ denote the transpose and the inverse of $\boldsymbol{a}$, respectively. $\mathrm{dev}(\boldsymbol{a}) = \boldsymbol{a} - \frac{1}{3}\,\mathrm{tr}\,(\boldsymbol{a})\mathbf{1}$ and $\mathrm{tr}(\boldsymbol{a}) = a_{ii}$ stand for the deviatoric part of and trace of $\boldsymbol{a}$, respectively, $\mathbf{1}$ denoting the identity tensor. $\mathrm{sym}(\boldsymbol{a})$ and $\mathrm{skw}(\boldsymbol{a})$ denote symmetric and skew-symmetric portions of $\boldsymbol{a}$. $\dot{\boldsymbol{a}}$ gives the material time derivative of $\boldsymbol{a}$. $\langle x\rangle = 1/2\big[x + |x|\big]$ describes the ramp function. The norm of $\boldsymbol{a}$ is denoted by $|\boldsymbol{a}| = \sqrt{\boldsymbol{a}\colon\boldsymbol{a}}$. Finally, ∇ is the material gradient operator.

Note that $\widehat{\mathcal{I}}^{\mathrm{dev}} \neq [\widehat{\mathcal{I}}^{\mathrm{dev}}]^n$ for $n>1$ and $\widehat{\mathcal{I}}^{\mathrm{dev}}$ is invertable, i.e., $\det(\widehat{\mathcal{I}}^{\mathrm{dev}}) \neq 0$. Let $\hat{\boldsymbol{\varepsilon}} \in \mathbb{S}$ denote the strain vector which only collects the in-plane components with $\hat{\boldsymbol{\varepsilon}} = \left[\varepsilon_{11}, \varepsilon_{22}, \sqrt{2}\varepsilon_{12}\right]^{\mathrm{T}}$. We assume the additivity of the total strain tensor into elastic $\hat{\boldsymbol{\varepsilon}}^e$ and plastic $\hat{\boldsymbol{\varepsilon}}^p$ parts viz. $\hat{\boldsymbol{\varepsilon}} = \hat{\boldsymbol{\varepsilon}}^e + \hat{\boldsymbol{\varepsilon}}^p$. For both $\hat{\boldsymbol{\varepsilon}}^e$ and $\hat{\boldsymbol{\varepsilon}}^p$ the same stencil applies.

The rate of stress tensor is then computed by $\hat{\dot{\boldsymbol{\sigma}}} = \widehat{\mathbb{C}}^e \cdot \hat{\dot{\boldsymbol{\varepsilon}}}^e$ where for the plane-stress case $\widehat{\mathbb{C}}^e$ reads

$$\widehat{\mathbb{C}}^e = \frac{E}{1-\nu^2}\begin{bmatrix} 1 & \nu & 0 \\ & 1 & 0 \\ \text{sym.} & & 1-\nu \end{bmatrix}. \tag{17}$$

$\hat{\boldsymbol{\chi}} = \left[\chi_{11}, \chi_{22}, \sqrt{2}\chi_{12}\right]^{\mathrm{T}}$ constitutes the vector representation for the kinematic hardening stress-like tensor $\hat{\boldsymbol{\chi}} \in \mathbb{S}^{\mathrm{dev}}$. Noting that $\overline{\boldsymbol{\chi}} = [\widehat{\mathcal{I}}^{\mathrm{dev}}]^{-1} \cdot \hat{\boldsymbol{\chi}} \in \hat{\mathbb{S}}$ we introduce $\hat{\boldsymbol{\xi}} := \hat{\boldsymbol{\sigma}} - \overline{\boldsymbol{\chi}}$. Accordingly, the plastic flow potential ϕ^p which accounts for isotropic-, kinematic- and cross-hardening is given as

$$\phi^p := \sqrt{\hat{\boldsymbol{\xi}} \cdot [\,\widehat{\mathcal{A}} + \widehat{\mathcal{H}}\,] \cdot \hat{\boldsymbol{\xi}}} - \sigma_y\left(e^p, \dot{e}^p\right) \leq 0. \tag{18}$$

In above, $\widehat{\mathcal{A}}$ and $\widehat{\mathcal{H}}$ denote the reduced plane-stress versions of the initial Hill-48-type [11] and the evolving 3×3 flow anisotropy matrices, respectively, with

$$\widehat{\mathcal{A}} = \begin{bmatrix} \mathcal{A}_{1111} & \mathcal{A}_{1122} & \sqrt{2}\mathcal{A}_{1112} \\ & \mathcal{A}_{2222} & \sqrt{2}\mathcal{A}_{2212} \\ \text{sym.} & & 2\mathcal{A}_{1212} \end{bmatrix} \quad \text{and}$$

$$\widehat{\mathcal{H}} = \begin{bmatrix} \mathcal{H}_{1111} & \mathcal{H}_{1122} & \sqrt{2}\mathcal{H}_{1112} \\ & \mathcal{H}_{2222} & \sqrt{2}\mathcal{H}_{2212} \\ \text{sym.} & & 2\mathcal{H}_{1212} \end{bmatrix}. \tag{19}$$

This notation leads to the following matrix form of the Hill-48-type structural tensor

$$\widehat{\mathcal{A}} = \begin{bmatrix} G+H & -H & 0 \\ & F+H & 0 \\ \text{sym.} & & N \end{bmatrix}, \tag{20}$$

where F, G, H and N are parameters associated with plastic anisotropy which are related to the Lankford's coefficients r_0, r_{45} and r_{90} with

$$F = \frac{r_0}{r_{90}[1+r_0]}, \quad G = \frac{1}{1+r_0}, \quad H = \frac{r_0}{1+r_0}, \quad N = \frac{1}{2}\frac{[r_0+r_{90}][1+2r_{45}]}{r_{90}[1+r_0]}. \tag{21}$$

In reduced plane-stress space, the vector norm of deviatoric tensors should be treated with care due to possible nonzero out-of-plane components. For the reduced deviatoric $\hat{\boldsymbol{\varepsilon}}^p$ the following identities hold for the quadratic forms in between the tensor and vector notations

$$\boldsymbol{\varepsilon}^p : \boldsymbol{\varepsilon}^p = \overline{\boldsymbol{\varepsilon}}^p \cdot \widehat{\mathcal{I}}^{\mathrm{dev}} \cdot \overline{\boldsymbol{\varepsilon}}^p = \hat{\boldsymbol{\varepsilon}}^p \cdot [\widehat{\mathcal{I}}^{\mathrm{dev}}]^{-1} \cdot \hat{\boldsymbol{\varepsilon}}^p, \tag{22}$$

$$\boldsymbol{n}^p : \boldsymbol{\mathcal{H}} : \boldsymbol{n}^p = \overline{\boldsymbol{n}}^p \cdot \widehat{\mathcal{H}} \cdot \overline{\boldsymbol{n}}^p, \tag{23}$$

where $\overline{\boldsymbol{\varepsilon}}^p = [\widehat{\mathcal{I}}^{\mathrm{dev}}]^{-1} \cdot \hat{\boldsymbol{\varepsilon}}^p$ and $\overline{\boldsymbol{n}}^p = [\widehat{\mathcal{I}}^{\mathrm{dev}}]^{-1} \cdot \hat{\boldsymbol{n}}^p$. The reduced evolution equation of the flow anisotropy tensor reads

$$\dot{\widehat{\mathcal{H}}}/\dot{e}^p = c_d[s_d \hat{\boldsymbol{n}}^p \otimes \hat{\boldsymbol{n}}^p - \widehat{\mathcal{H}}^d] + c_l[s_l[\widehat{\mathcal{I}}^{\mathrm{dev}} - \hat{\boldsymbol{n}}^p \otimes \hat{n}^p] - \widehat{\mathcal{H}}^l], \tag{24}$$

with

$$\hat{\boldsymbol{n}}^p \otimes \hat{\boldsymbol{n}}^p = \begin{bmatrix} n_{11}^p n_{11}^p & n_{11}^p n_{22}^p & \sqrt{2} n_{11}^p n_{12}^p \\ & n_{22}^p n_{22}^p & \sqrt{2} n_{22}^p n_{12}^p \\ \text{sym.} & & 2 n_{12}^p n_{12}^p \end{bmatrix}, \tag{25}$$

where

$$\widehat{\mathcal{H}}^d = [\overline{\boldsymbol{n}}^p \cdot \widehat{\mathcal{H}} \cdot \overline{\boldsymbol{n}}^p]\left[\hat{\boldsymbol{n}}^p \otimes \hat{\boldsymbol{n}}^p\right] \quad \text{and} \quad \widehat{\mathcal{H}}^l = \widehat{\mathcal{H}} - \widehat{\mathcal{H}}^d. \tag{26}$$

In Fig. 2 the evolution of the yield loci for various strain paths for an initially isotropic material are given using the presented theory for the case of plane-stress. In this analysis any further hardening source except latent hardening are switched off. It is clearly seen that for each case the yield locus curvature at the point of loading decreases. This behavior is contrary to what is generally observed in metallic materials showing vertex formation, which gives relatively reduced formability limits [35,26,27]. In the subsequent pages we investigate the effect of this curvature decrease making use of basic formability tests.

4. Algorithmic formulation and verification of the implementation

In this part, we summarize the return mapping algorithm used to define the state variables at the end of loading step $n+1$, that is $[\bullet]^{\langle n+1\rangle}$, using the state variables at the end of loading step n, that is $[\bullet]^{\langle n\rangle}$, through a strain driven framework using a cutting plane algorithm [30]. To this end, we linearize the flow potential around the current values of variables viz.

$$\phi^p_{\langle k+1\rangle} \simeq \phi^p_{\langle k\rangle} + \hat{\boldsymbol{r}}_{\langle k\rangle} \cdot \delta\hat{\boldsymbol{\sigma}}_{\langle k\rangle} + \overline{\boldsymbol{s}}_{\langle k\rangle} \cdot \delta\overline{\boldsymbol{\chi}}_{\langle k\rangle} + \widehat{\mathcal{D}}_{\langle k\rangle} : \delta\widehat{\mathcal{H}}_{\langle k\rangle} + \varsigma_{\langle k\rangle}\delta e^p_{\langle k\rangle} + \vartheta_{\langle k\rangle}\delta\dot{e}^p_{\langle k\rangle}, \tag{27}$$

with k denoting the iteration number and $\hat{\boldsymbol{r}} = \partial\phi^p/\partial\hat{\boldsymbol{\sigma}}$, $\overline{\boldsymbol{s}} = \partial\phi^p/\partial\overline{\boldsymbol{\chi}}$, $\widehat{\mathcal{D}} = \partial\phi^p/\partial\widehat{\mathcal{H}}$, $\varsigma = \partial\phi^p/\partial e^p$ and $\vartheta = \partial\phi^p/\partial\dot{e}^p$ where

$$\hat{\boldsymbol{r}}\sigma_y = [\widehat{\mathcal{A}} + \widehat{\mathcal{H}}] \cdot \hat{\boldsymbol{\xi}}, \tag{28}$$

$$\overline{\boldsymbol{s}} = -\hat{\boldsymbol{r}}, \tag{29}$$

$$\widehat{\mathcal{D}}\sigma_y = [\widehat{\mathcal{I}}^{\mathrm{dev}} \cdot \hat{\boldsymbol{\xi}}] \otimes [\widehat{\mathcal{I}}^{\mathrm{dev}} \cdot \hat{\boldsymbol{\xi}}] = [\mathrm{dev}(\hat{\boldsymbol{\sigma}}) - \hat{\boldsymbol{\chi}}] \otimes [\mathrm{dev}(\hat{\boldsymbol{\sigma}}) - \hat{\boldsymbol{\chi}}], \tag{30}$$

$$\varsigma = -h'_y r_y, \tag{31}$$

$$\vartheta = -h_y r'_{\dot{y}}. \tag{32}$$

Using $\hat{\boldsymbol{n}}_{\langle k\rangle} = \hat{\boldsymbol{r}}_{\langle k\rangle}/\sqrt{\hat{\boldsymbol{r}}_{\langle k\rangle} \cdot [\widehat{\mathcal{I}}^{\mathrm{dev}}]^{-1} \cdot \hat{\boldsymbol{r}}_{\langle k\rangle}}$, the increments within iterations read

$$\delta\hat{\boldsymbol{\sigma}}_{\langle k\rangle}/\delta e^p_{\langle k\rangle} = -\widehat{\mathbb{C}}^e \cdot \hat{\boldsymbol{r}}_{\langle k\rangle}, \tag{33}$$

$$\delta\overline{\boldsymbol{\chi}}_{\langle k\rangle}/\delta e^p_{\langle k\rangle} = c_\chi\,[\widehat{\mathcal{I}}^{\mathrm{dev}}]^{-1} \cdot [s_\chi \hat{\boldsymbol{n}}^p_{\langle k\rangle} - \hat{\boldsymbol{\chi}}_{\langle k\rangle}], \tag{34}$$

$$\delta\widehat{\mathcal{H}}_{\langle k\rangle}/\delta e^p_{\langle k\rangle} = c_d\left[s_d \hat{\boldsymbol{n}}^p_{\langle k\rangle} \otimes \hat{\boldsymbol{n}}^p_{\langle k\rangle} - \widehat{\mathcal{H}}^d_{\langle k\rangle}\right] + c_l\left[s_l\left[\widehat{\mathcal{I}}^{\mathrm{dev}} - \hat{\boldsymbol{n}}^p_{\langle k\rangle} \otimes \hat{\boldsymbol{n}}^p_{\langle k\rangle}\right] - \widehat{\mathcal{H}}^l_{\langle k\rangle}\right], \tag{35}$$

$$\delta\dot{e}^p_{\langle k\rangle}/\delta e^p_{\langle k\rangle} \simeq 1/\Delta t. \tag{36}$$

Iterations are started by defining $[\bullet]_{\langle 0\rangle} = [\bullet]^{\langle n\rangle}$. We compute the increment of equivalent plastic strain at each iteration by

$$\delta e^p_{\langle k\rangle} = \frac{\phi^p_{\langle k\rangle}}{\hat{\boldsymbol{r}}_{\langle k\rangle} \cdot \widehat{\mathbb{C}}^e \cdot \hat{\boldsymbol{r}}_{\langle k\rangle} + \hat{\boldsymbol{r}}_{\langle k\rangle} \cdot [\widehat{\mathcal{I}}^{\mathrm{dev}}]^{-1} \cdot \left[c_\chi[s_\chi \hat{\boldsymbol{n}}^p_{\langle k\rangle} - \hat{\boldsymbol{\chi}}_{\langle k\rangle}]\right] - \widehat{\mathcal{D}}_{\langle k\rangle} : \left[\delta\widehat{\mathcal{H}}_{\langle k\rangle}/[\delta e^p_{\langle k\rangle}\sigma_{y\langle k\rangle}]\right] - \varsigma_{\langle k\rangle} - \vartheta_{\langle k\rangle}/\Delta t}. \tag{37}$$

Iterations are continued to update the state variables using

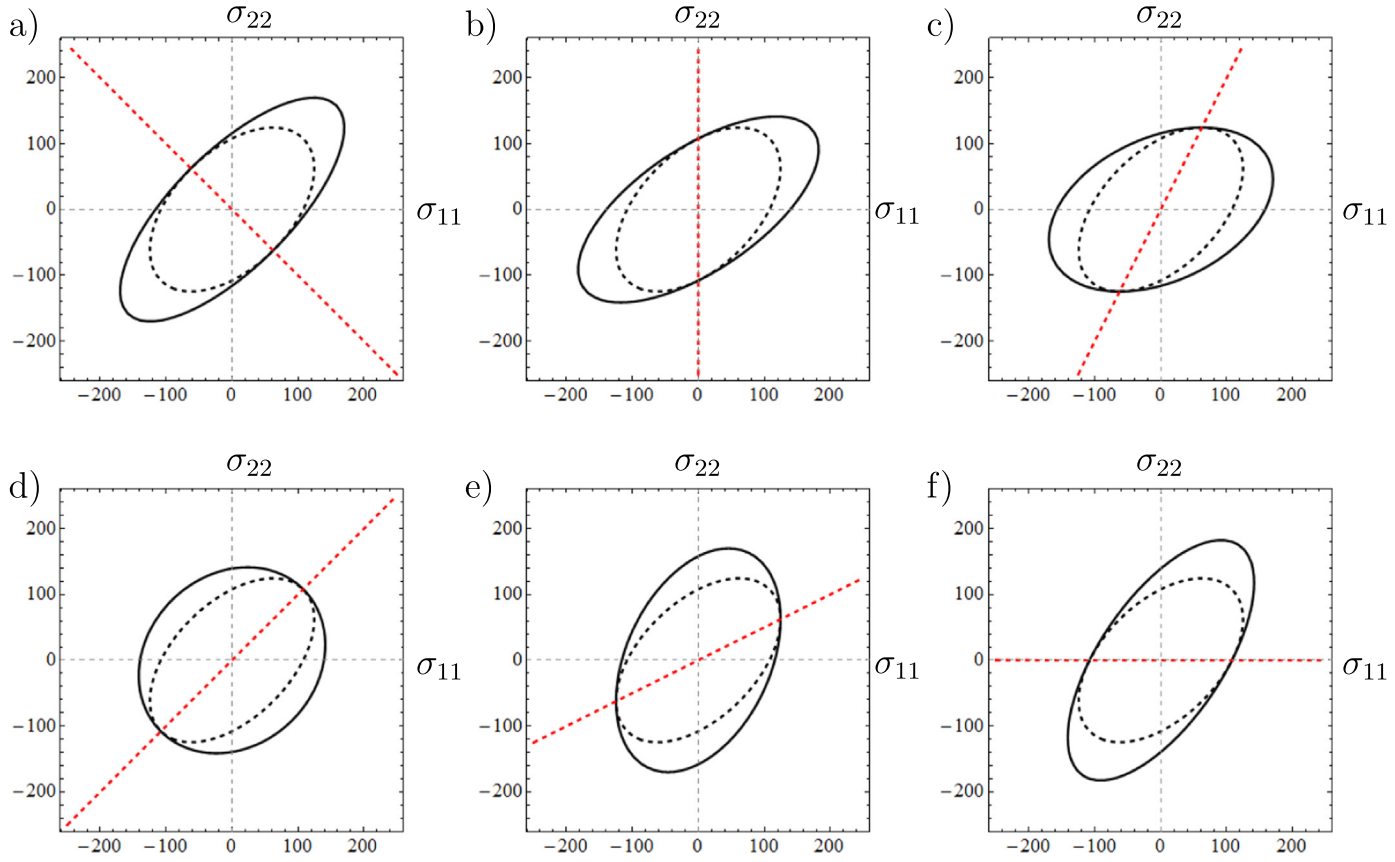

Fig. 2. Plane-stress yield loci evolution for various loading paths. Dashed curves refer to the initial yield loci whereas black curves refer to the current one after deformation under a linear strain (stress) path marked by the dashed red line; a) pure shear, b) uniaxial tension-compression, c) plane strain tension-compression, d) equibiaxial tension-compression, e) plane strain tension-compression, f) uniaxial tension-compression. In all cases the yield locus curvature at the point of loading decreases. This is governed principally by the rotation and the aspect ratio change of the representing ellipses. For the pure shear and equibiaxial stress paths, no rotation of the ellipse axes takes place. (For interpretation of the references to color in this figure legend, the reader is referred to the web version of this article.)

$[\bullet]_{\langle k+1\rangle} = [\bullet]_{\langle k\rangle} + \delta[\bullet]_{\langle k\rangle}$ until $\phi^p \leq \text{TOL}$. The converged state gives the solution at the end of the loading step $n+1$ with $[\bullet]^{\langle n+1\rangle} = [\bullet]_{\langle k+1\rangle}$ where the increments read $\Delta[\bullet] = [\bullet]^{\langle n+1\rangle} - [\bullet]^{\langle n\rangle}$. The out-of-plane strain increment is then defined using $\Delta\hat{\varepsilon}_{33} \equiv \Delta\hat{\varepsilon}^e_{33} + \Delta\hat{\varepsilon}^p_{33}$ and $\Delta\hat{\boldsymbol{\varepsilon}}^p = \Delta\varepsilon^p\,\hat{\boldsymbol{r}}$ viz.

$$\Delta\hat{\varepsilon}^e_{33} = -\frac{\nu}{1-\nu}\left[\Delta\hat{\varepsilon}^e_{11} + \Delta\hat{\varepsilon}^e_{22}\right], \quad \text{and} \quad \Delta\hat{\varepsilon}^p_{33} = -\left[\Delta\hat{\varepsilon}^p_{11} + \Delta\hat{\varepsilon}^p_{22}\right]. \tag{38}$$

Here ν denotes elastic Poisson's ratio. The developed algorithm is implemented as a VUMAT user defined material subroutine in Abaqus. A comparison of the implementation via Voigt and Mandel vector notation are given in Appendix A. Appendix B presents the extension to finite strains of the presented small strain theory.

4.1. Verification of the implementation

We verify the implementation using two problems: finite strain in-plane loading with non-rotating principal axes of deformation and small strain in-plane shear loading. The numerical solutions with single element tests are compared with fully analytical derivations which appear in the literature for the first time.

4.1.1. Finite strain in-plane loading with non-rotating axes of deformation

We assume rigid plasticity with $[\varepsilon_{11}, \varepsilon_{22}, \varepsilon_{33}]^\top \simeq [\varepsilon^p_{11}, \varepsilon^p_{22}, \varepsilon^p_{33}]^\top$. Strain controlled loading is applied where the in-plane strains in $x-$ and $y-$ directions are defined and the out-of-plane strain is found using the other two using the assumptions of isochoric plastic flow. Only strictly proportional strain paths are considered, that is $\alpha = d\varepsilon_{11}/d\varepsilon_{22} = \varepsilon_{11}/\varepsilon_{22}$. Hence, the total strain vector $\boldsymbol{\varepsilon}$ reads $\boldsymbol{\varepsilon} = [\alpha, 1, -1-\alpha]^\top$. The mentioned in-plane loading condition with non-rotating axis of deformation allows an immediate integration of the structural tensor to give the following normal components for $s_d{=}0$ (see [34] for more details)

$$\mathcal{H}_{1111}(\gamma) = s_l f_{c_l}\left[\frac{2}{3} - \frac{\alpha^2}{2[1+\alpha+\alpha^2]}\right], \tag{39}$$

$$\mathcal{H}_{1122}(\gamma) = s_l f_{c_l}\left[-\frac{1}{3} - \frac{\alpha}{2[1+\alpha+\alpha^2]}\right], \tag{40}$$

$$\mathcal{H}_{2222}(\gamma) = s_l f_{c_l}\left[\frac{2}{3} - \frac{1}{2[1+\alpha+\alpha^2]}\right], \tag{41}$$

where $f_{c_l}(\gamma) = 1 - \exp(-c_l\,\gamma)$. In this $xy-$ plane loading, the shear component H_{1212} also evolves with

$$\mathcal{H}_{1212}(\gamma) = \frac{s_l}{2}\left[1 - \exp(-c_l\gamma)\right], \tag{42}$$

for $s_d{=}0$. A comparison of the analytical derivation and the numerical result of a single element test is given in Fig. 3 where a perfect agreement is observed.

4.1.2. Small strain in-plane shear loading

Assuming small shear strains in the $xy-$ plane, the only nonzero strain components become $\varepsilon^p_{12} = \varepsilon^p_{21}$. This allows deriving the following expression for H_{1212} for $s_d \neq 0$ through integration

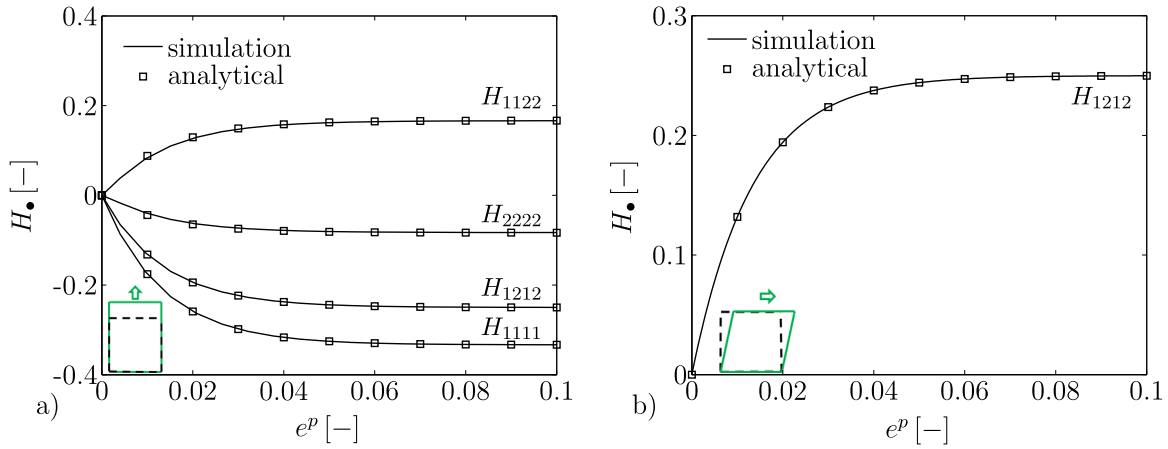

Fig. 3. Comparison of analytical and numerical results for the evolving structural tensor $\mathcal{H}$ for a) normal loading case with finite strain assumption, b) shear loading case with small strain assumption. Both the normal loading and shear loading cases used parameters are listed in Table 1 with one exception that in the shear test s_d=0.5 is used.

$$\mathcal{H}_{1212}(\gamma) = \frac{s_d}{2}\Big[1 - \exp\big(-c_d\gamma\big)\Big]. \tag{43}$$

A perfect agreement is observed for the comparison of the analytical derivation and the numerical result of a single element test in Fig. 3.

5. Applications – formability analyses

In this section we present the formability prediction of cross hardening plasticity in comparison to non-cross hardening material models. We start with Marciniak-Kuczyńsky-type of analyses where a biaxial loading of a defected rectangular plate is analyzed under various strain paths to form the first quadrant of the forming limit diagram. Unlike conventional Marciniak-Kuczyńsky test which uses an oriented groove in the model we consider randomly distributed spatially correlated defects to trigger localization. The second application problem consists of the Nakazima test where a sheet with various cut geometries is stretched with a punch moving perpendicular to the plane of the sheet. Both formability analyses are realized using the finite element method. Both analyses show that with the decrease of yield locus curvature, cross hardening plasticity predicts a later localization and therefore an increase in formability.

In the analyses, the parameter set listed in Table 1 is used unless otherwise stated. In order to purely concentrate on the cross hardening effects, the rate parameter is chosen to yield vanishing rate dependence. With selecting Lankford's coefficients as $r_0 = r_{45} = r_{90} = 1$ we assume initial plastic isotropy.

5.1. Marciniak-Kuczyńsky test simulations

The formability of the metallic sheets is determined by a localized through-thickness neck formation along a zero-extension direction which is often preceded by a diffuse neck. For the loading states involving two positive in-plane strains, however, no zero extension direction exists. Based on experimental results regarding strain localization, it was concluded by Marciniak and Kuczyński [24] that failure or necking is mostly initiated by geometrical or structural in homogeneities. Hence, for the localization to develop in the first quadrant of the forming limit diagram, presence of imperfections was postulated to be responsible in Marciniak-Kuczyńsky theory. The original Marciniak-Kuczyńsky analysis is, in order to allow fast analytical or semi-analytical solutions, based on two simplifying assumptions: 1) The defect considered is infinite in length. 2) Boundary conditions are assigned considering constant bulk stress paths [39]. A joint use of the finite element method with stochastically generated material defect distribution makes it possible to avoid these over-simplifications, hence allow a more realistic production of the forming limit diagrams. Fig. 4a) shows the simulation set-up for the Marciniak-Kuczyńsky test. The plate is loaded under biaxial in-plane loading conditions considering totally six true strain (rate) ratios $\dot{\varepsilon}_2/\dot{\varepsilon}_1 \in \{0, 0.2, 0.4, 0.6, 0.8, 1.0\}$ which allows plotting forming limit diagram points corresponding to the first quadrant ($\dot{\varepsilon}_2$ serves as major strain rate.). For post processing reasons the specimen is subdivided into 10×10 different cells with aspect ratio 1:1. The chosen discretization and subdivision prevent any sensitivity of the FEM results (see [29]).

In the model proposed by Marciniak and co-workers [24,25], a thickness variation in a distinct region as geometrical inhomogeneity is introduced. The necking or failure behavior is analyzed on basis of the principal strains in these two regions of different thicknesses of the specimen subjected to a biaxial stress state. Using finite element analysis, Narasimhan and Wagoner [29] suggested three simple criteria to identify the point of failure of such specimens to determine the formability capabilities of the material on basis of the ratio of the major or minor principal strain rates or the effective strain rates of both regions. We account for a random initial yield stress distribution

Table 1
Material parameters, representing approximately steel.

	Symbol	Value	Dimension
Elastic constants	μ	69.6	[GPa]
	K	150.8	[GPa]
Isotropic hardening constants	σ_{y0}	132.2	[MPa]
	σ_∞	324.0	[MPa]
	m	6.6	[−]
	n	1	[−]
	$r_y(\dot{e}^p)$	1	[−]
Kinematic hardening constants	s_x	56.0	[MPa]
	c_x	33.1	[−]
Lankford's coefficients	r_0	1	[−]
	r_{45}	1	[−]
	r_{90}	1	[−]
Cross hardening constants	s_d	0.0	[−]
	c_d	23.9	[−]
	s_l	−0.9	[−]
	c_l	87.3	[−]

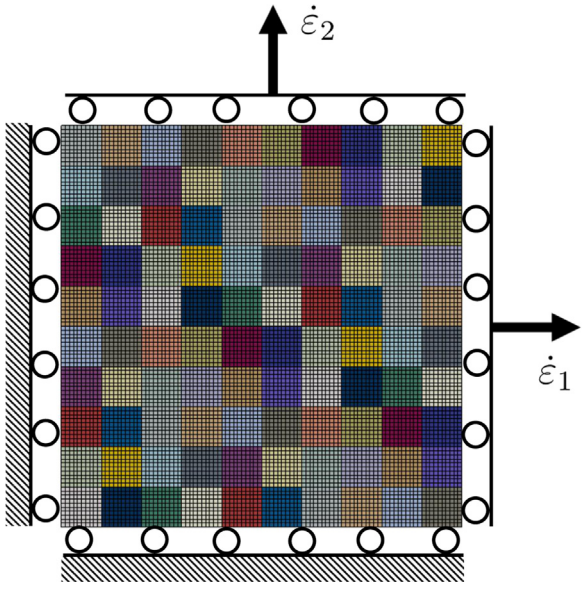

Fig. 4. Finite element analysis of the Marciniak-Kuczyńsky test: Simulation set-up representing the metal sheet/plate, a 2-dimensional $[0, L] \times [0, L]$ domain. True strain rates $(\dot{\varepsilon}_1,\ \dot{\varepsilon}_2)$ are applied to load the plate under biaxial in-plane loading conditions. The strain rates are adjusted according to the investigated strain paths. The sample is subdivided into 100 cells with aspect ratio of 1:1. For each of these cells the average major, minor and equivalent plastic strain rates $(\dot{\varepsilon}_2,\ \dot{\varepsilon}_1,\ \dot{\varepsilon}^p)$ are calculated which are used for evaluation of the different formability criteria.

with a given correlation where the total yield stress distribution function is assumed to be

$$\sigma_{y0}(\boldsymbol{r}) = \sigma_{y0,u} + \sigma\, \widetilde{X}_{\boldsymbol{r}}, \tag{44}$$

where σ is the standard deviation of the yield stress which is superimposed over the base uniform yield stress distribution $\sigma_{y0,u}$. $\{\widetilde{X}_{\boldsymbol{r}}\}$ represents a stationary Gaussian random field with zero mean and unit variance generated on each of the grid points $\{(i, j)/n, i = 0, 1, \ldots, n-1, j = 0, 1, \ldots, n-1\}$ corresponding to a Gaussian covariance function of the form

$$\mathrm{Cov}(\widetilde{X}_{\boldsymbol{r}}, \widetilde{X}_{\boldsymbol{s}}) = \phi(\boldsymbol{r} - \boldsymbol{s}) = \exp\left(\frac{-|\boldsymbol{r} - \boldsymbol{s}|^2}{L_c^2}\right). \tag{45}$$

Here, $\boldsymbol{r}$ and $\boldsymbol{s}$ represent position vectors with $|\boldsymbol{r} - \boldsymbol{s}|^2 = [r_1 - s_1]^2 + [r_2 - s_2]^2$ and with L_c corresponding to the (isotropic) correlation length. Using $L_c = L/10$, 12 realizations of the stationary Gaussian random field $\{\widetilde{X}_{\boldsymbol{r}}\}$ with $\mathcal{N}[0, 1]$ are produced as shown in Fig. 5. The statistics of each realization is given in Table 2. Details of the method of generation the random field distribution with a given correlation are given in the Appendix C.

The previous described discretization into cells of the finite element model (see Fig. 4b) is advantageous for the post-calculation of an appropriate failure criteria in stochastic simulations as the results no longer depend on the choice of one specific element for the evaluation of the failure criteria. For the following criteria, the different strain rates are averaged for each cell. Following

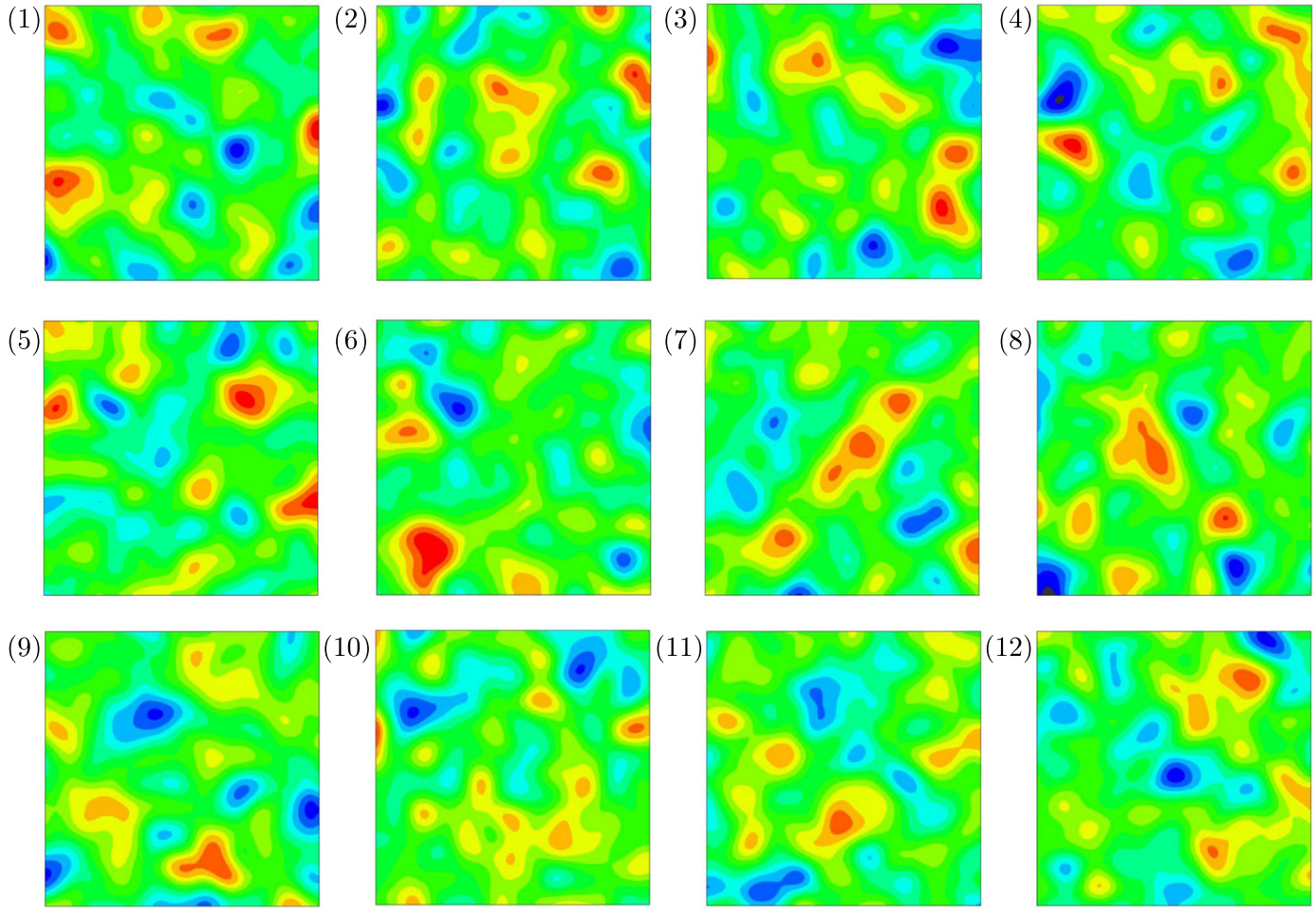

Fig. 5. 12 realizations of the stationary Gaussian random field $\{\widetilde{X}_{\boldsymbol{r}}\}$ with $\mathcal{N}[0, 1]$, i.e., zero mean and unit variance. Correlation length of $L_c = L/10$ for the 2-dimensional $[0, L] \times [0, L]$ domain. (max, min) = (3.25, − 3.25). Yield stress distributions are then computed using $\sigma_{y0}(\boldsymbol{r}) = \sigma_{y0,u} + \sigma\widetilde{X}_{\boldsymbol{r}}$, Eq. (44), with $\sigma_{y0,u} = 132.19$ MPa and $\sigma = 2.5\% \times \sigma_{y0,u} \simeq 3.305$ MPa as the standard deviation of the yield stress distribution. The statistics of each realization are given in Table 2.

Table 2
Statistics of each realization shown in Fig. 5.

ID	Mean	std.dev.=[variance]$^{1/2}$
1	0.0041	0.9873
2	−0.0107	0.9908
3	−0.0010	1.0122
4	−0.0018	1.0105
5	0.0077	0.1003
6	0.0104	0.9869
7	0.0101	0.9888
8	0.0159	1.0075
9	−0.0006	1.0153
10	0.0244	0.9778
11	−0.0119	0.9873
12	−0.0209	1.0027

Narasimhan and Wagoner [29], three criteria on basis of different strain rates are adopted. Additionally a criterion on basis of the stress is introduced. The first criterion, the major strain rate criterion $c_{\dot{\varepsilon}_2}$,

$$c_{\dot{\varepsilon}_2} = \frac{\text{largest major strain rate}(\dot{\varepsilon}_2)\text{in one cell}}{\text{smallest major strain rate}(\dot{\varepsilon}_2)\text{in one cell}} \geq 10 = c_{\dot{\varepsilon}_2,\text{threshold}}, \tag{46}$$

calculates the ratio of largest major strain rate to smallest major strain rate in one of the different cells. As strain localization occurs very localized in one or only a few cells, the largest major strain rate is present in the cell of localization. This is usually happening in the weakest point of the sheet, here determined by the lowest yield strength within the specimen. On the other hand, a strain rate similar to the smallest strain rate is found in the remaining cells. As soon as a characteristic threshold $c_{\dot{\varepsilon}_2,\text{threshold}}$ is reached, the point of flow localization can be identified. The second criterion, the minor strain criterion $c_{\dot{\varepsilon}_1}$, reads as:

$$c_{\dot{\varepsilon}_1} = \frac{\text{largest minor strain rate}(\dot{\varepsilon}_1)\text{in one cell}}{\text{smallest minor strain rate}(\dot{\varepsilon}_1)\text{in one cell}} \geq 10 = c_{\dot{\varepsilon}_1,\text{threshold}}. \tag{47}$$

This criterion fails under plane strain loading as $\dot{\varepsilon}_{1\,\min} = 0$. The third strain rate criterion ($c_{\dot{e}^p}$) is based on the equivalent plastic strain rate:

$$c_{\dot{e}^p} = \frac{\text{largest equivalent plastic strain rate}(\dot{e}^p)\text{in one cell}}{\text{smallest equivalent plastic strain rate}(\dot{e}^p)\text{in one cell}} \geq 4 = c_{\dot{e}^p,\text{threshold}}. \tag{48}$$

As noted by [29], these three criteria show typically little variance of identifying the corresponding strains at strain localization. In addition to these three criteria, we propose a new criterion, the effective stress criterion c_σ, which does not require local information of the structure, rather the information at the boundary. This criterion reads:

$$c_\sigma = \text{true effective stress}\left(\sqrt{\sigma_1^2 + \sigma_2^2}\right) \leq c_{\sigma,\text{threshold}} = 0.98\,\sigma_{\max} \quad \text{and} \quad \dot{\sigma} \leq 0. \tag{49}$$

It identifies the strain localization on basis of a negative stress rate in combination with a reduction of the stress by a certain percentage, here 2%, from its maximum value.

Calculations with the 12 realizations of the stationary Gaussian random field $\{\bar{X}_{\mathbf{r}}\}$ with $\mathcal{N}[0, 1]$ as shown in Fig. 5 were performed for each of the strain ratios for the cross-hardening plasticity model. Figs. 6 and 7show, for a selected random initial yield stress distribution, the evolution of localized equivalent plastic strains under two strain paths: plane strain tension and equibiaxial tension. Both localization patterns are strongly influenced by the underyling initial yield stress distribution. In both cases the deformation bands initiate at points where the hardening source is exhausted. These correspond to regions with relatively lower initial yield stresses, the so-called defected regions. The responses for both strain paths show different characteristics. In plane strain tension, localization initiates at much earlier strains and the band develops orthogonal to the loading direction. Since localized neck occurs along a zero extension direction, this shows that in plane strain tension no path change occurs in the band during loading. Hence, in absence of loading path change, there is no effect of yield locus curvature on the localization. In the biaxial loading case, this is not the case. Prior to localized necking, the loading path is characterized by two positive in-plane strains. During neck development, there occurs a continuous strain path change from equibiaxial to plane strain to create a zero extension direction along the localization band. For an associated plastic flow, the local curvature of the yield locus at the loading point, thus, affects the response of the sheet. For lower local curvature due to cross hardening plasticity then leads to a more stable material response where the rotation of the normal becomes relatively harder. This observation is valid for all biaxial tensile loading paths with $\dot{\varepsilon}_2/\dot{\varepsilon}_1 > 0$. Moreover, as compared to the plane strain loading path the point of localization initiation is delayed. The final pattern does not emerge as a single band which traverses the whole domain but rather branches into secondary bands.

The response of the different criteria, normalized w.r.t. to the corresponding threshold value is shown in Fig. 8. As for plane strain loading, the minor strain criterion fails as expected. All remaining three criteria predict a fairly similar value for the

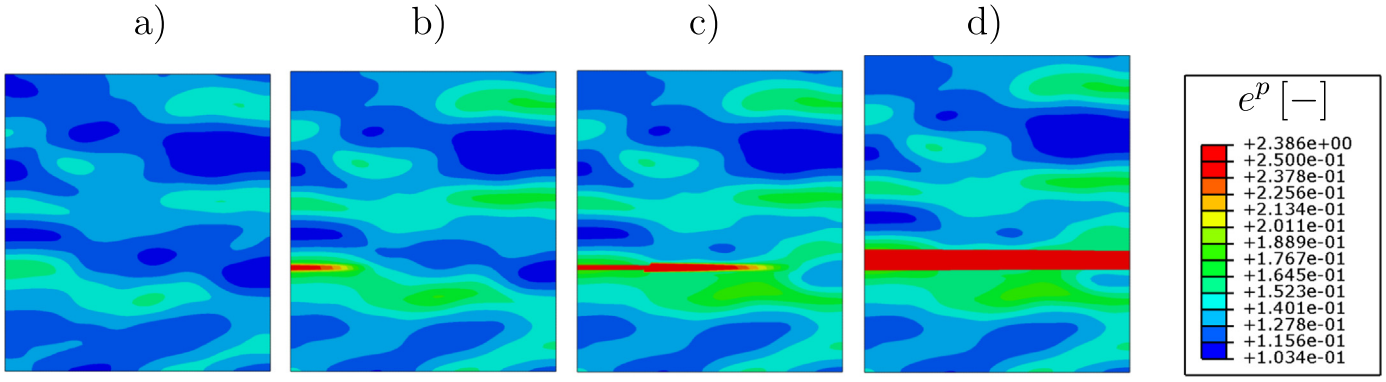

Fig. 6. Marciniak-Kuczyńsky test simulations, cross-hardening plasticity model: Evolution of localized plastic strain e^p in metal sheet with random defect distribution realization 5 (see Fig. 5) at strains a) $\varepsilon_2 = 0.116$, b) $\varepsilon_2 = 0.127$, c) $\varepsilon_2 = 0.133$, d) $\varepsilon_2 = 0.191$, under plane strain loading. In the plane strain loading condition the band emerges orthogonal to the loading direction.

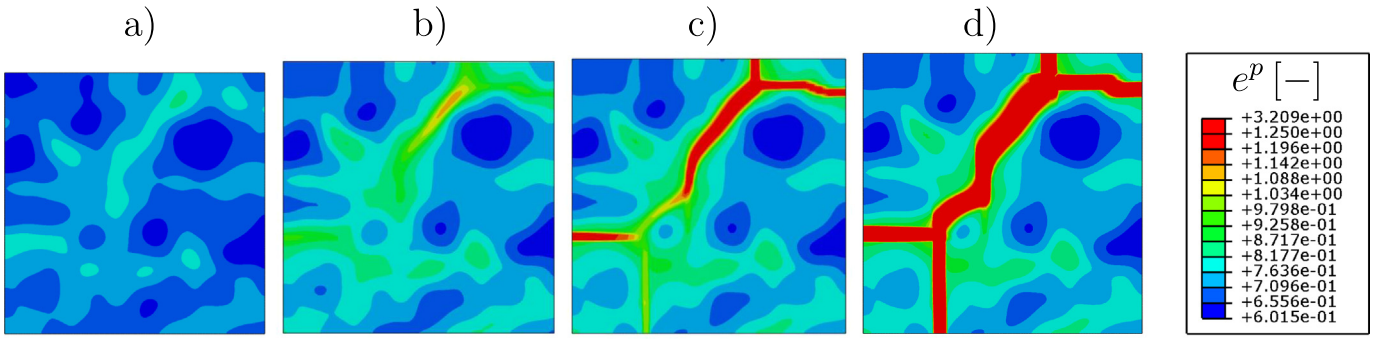

Fig. 7. Marciniak-Kuczyńsky test simulations, cross-hardening plasticity model: Evolution of localized equivalent plastic strain e^p in metal sheet with random defect distribution realization 5 (see Fig. 5) at strains a) $\varepsilon_2 = 0.405$, b) $\varepsilon_2 = 0.462$, c) $\varepsilon_2 = 0.477$, d) $\varepsilon_2 = 0.507$, under equibiaxial stretching. In the equibiaxial loading condition, a diagonal band initiation is followed by band branching/merging. Considerably higher strain values at localization are observed as compared to plane strain loading.

localization strain ε_2. For equibiaxial stretching, the equivalent strain rate predicts localization as first, followed by the major strain rate criteria and minor strain rate criterion. The stress criteria detects the localization at last. However, the differences are still rather small, all four criteria are acceptable for the identification of the material formability. In the following, the results are shown for the equivalent plastic strain rate criterion $c_{\dot{e}^p}$.

Fig. 9 summarizes emerging localization patterns for different loading conditions. Due to the stochastic defect distribution, the resulting localization patterns are complex as the nucleation might simultaneously occur at several positions in the specimen. The figures clearly show the relative localization tolerance of the plate to the applied loading path: least formability is observed in the plane strain loading case whereas most formability is recorded for the case of equibiaxial loading. Also, as anticipated, in the absence of loading path change in the band, there is no effect of yield locus curvature on the localization for plane strain loading case. Thus, in plane strain loading path, we record identical responses for the models with and without cross hardening.

The resulting first quadrant of the forming limit diagram obtained from the Marciniak-Kuczyńsky test for different simulation cases are displayed in Fig. 10. Results for cross hardening plasticity and non-cross hardening material models are shown for 12 realizations for each loading path. In total, the figure includes the results of $12 \times 6 \times 2 = 144$ simulations. A critical amount of localization needs to be recorded in the stochastic simulations before the criteria detect the material formability limit. The results with cross-hardening (cross) and non-cross-hardening (non-cross) material models have overlaps due to the effect of varying defect sizes in different realizations, however, the mean curves show a clear separation. For the plane strain path, both models predict the same formability as anticipated. For all other strain paths, the results demonstrate the improved formability due to cross-hardening. The explanation is the local curvature of the yield locus at the loading point whose decrease impedes the rotation of the normal for associated plastic flow and thus increases the stability. Fig. 10 shows that for all biaxial tensile loading paths with $\dot{\varepsilon}_2/\dot{\varepsilon}_1 > 0$ this observation preserves validity where the curvature effect of the cross hardening plasticity gets more prononunced as the ratio $\dot{\varepsilon}_2/\dot{\varepsilon}_1 \leq 1$ gets higher.

5.2. Nakazima test simulations

As a second application problem, Nakazima tests are performed to identify the formability of the material for different stress states [28]. The test set-up is similar to deep-drawing where the metal sheet is deformed using a hemispherical punch moving perpendicular to the plane of the sheet. Different stress states are achieved by using metal sheets with different cut geometries. The geometry of the metal sheet is shown in Fig. 11a) where circles of different radii are cut from the entire blank leading to strongly waisted blanks (see Fig. 12). Depending on the cutting radius,

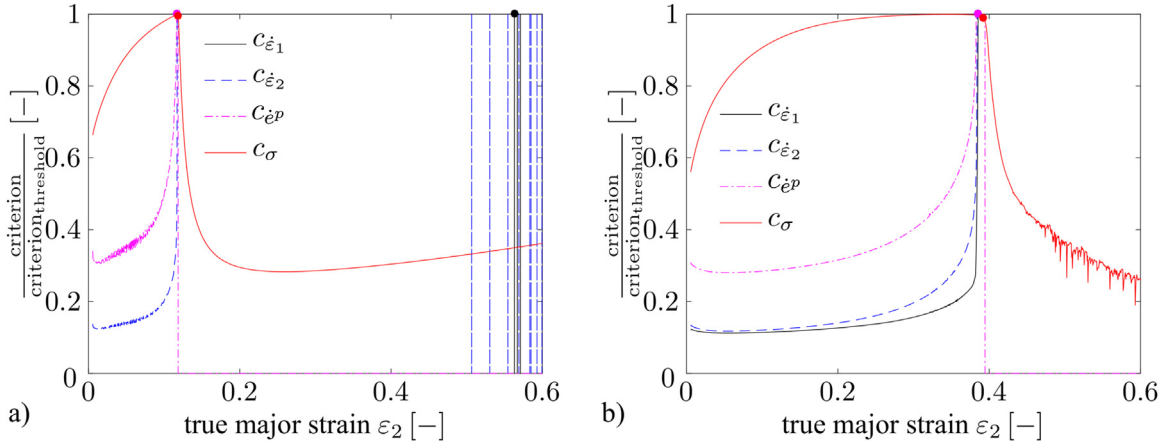

Fig. 8. Marciniak-Kuczyńsky test simulations, cross-hardening plasticity model: Normalized prediction of material formability by major strain rate criterion ($c_{\dot{\varepsilon}_2}$), minor strain rate criterion ($c_{\dot{\varepsilon}_1}$), equivalent plastic strain rate criterion $c_{\dot{e}^p}$ and stress criterion c_σ for a) plane strain loading and b) equibiaxial stretching. All criteria are normalized by its corresponding threshold value $c_{\bullet,\text{threshold}}$. The minor strain criterion fails for plane strain loading. Otherwise, all four criteria predict a similar formability.

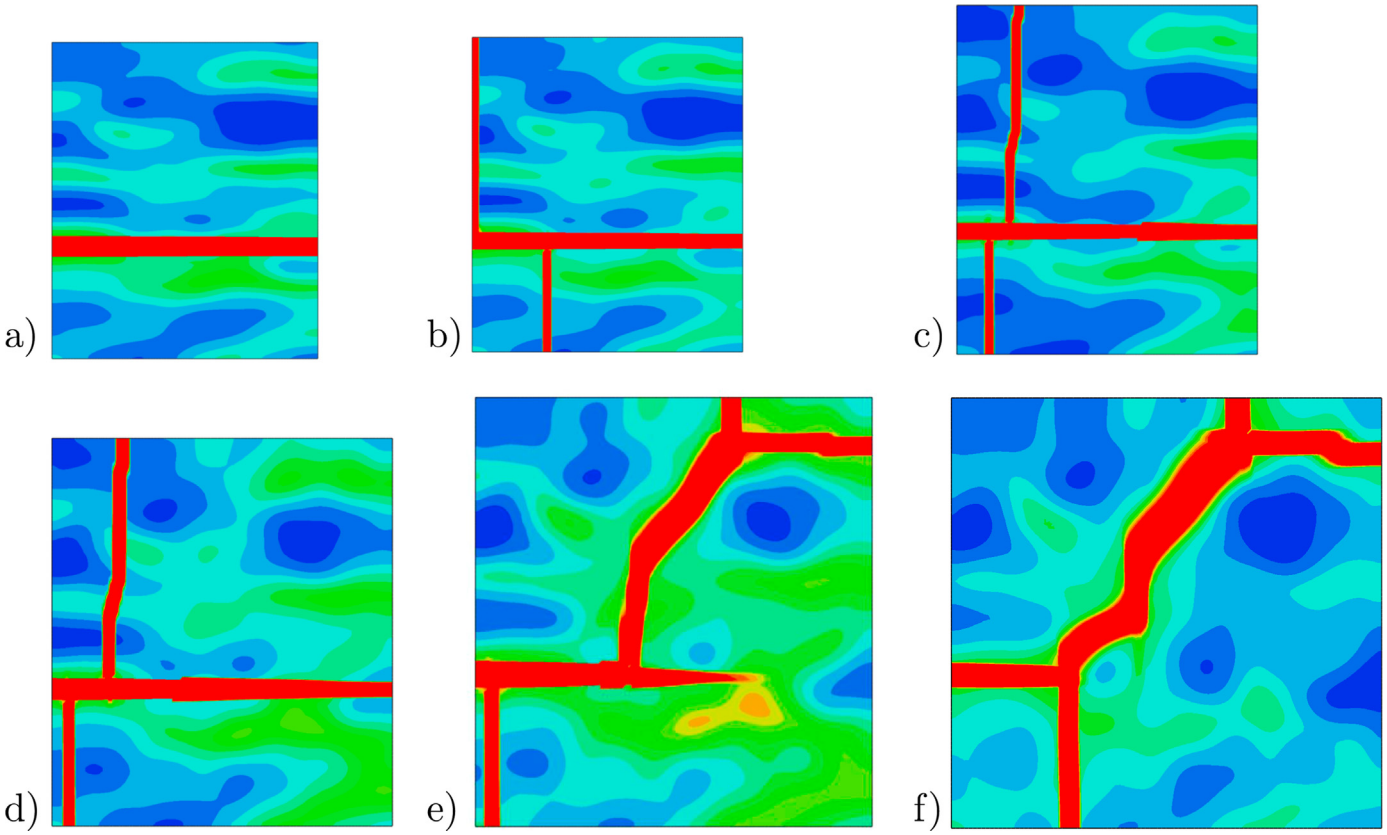

Fig. 9. Marciniak-Kuczyńsky test simulations, cross-hardening plasticity model: final plastic strain e^p localization patterns in metal sheet with random defect distribution realization 5 (see Fig. 5) under various loading conditions: a) Strain ratio of $\dot{\varepsilon}_2/\dot{\varepsilon}_1 = 0$ at $\varepsilon_2 = 0.191$; b) Strain ratio of $\dot{\varepsilon}_2/\dot{\varepsilon}_1 = 0.2$, at $\varepsilon_2 = 0.209$; c) Strain ratio of $\dot{\varepsilon}_2/\dot{\varepsilon}_1 = 0.4$, at $\varepsilon_2 = 0.284$; d) Strain ratio of $\dot{\varepsilon}_2/\dot{\varepsilon}_1 = 0.6$, at $\varepsilon_2 = 0.391$; e) Strain ratio of $\dot{\varepsilon}_2/\dot{\varepsilon}_1 = 0.8$, at $\varepsilon_2 = 0.484$; f) Strain ratio of $\dot{\varepsilon}_2/\dot{\varepsilon}_1 = 1.0$, at $\varepsilon_2 = 0.507$. The results show the effect of the stochastic distribution of defects. With increasing strain rate ratio, the formability increases.

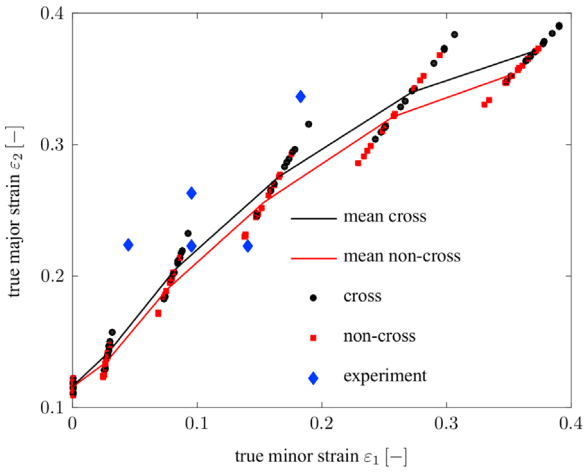

Fig. 10. Marciniak-Kuczyńsky test simulations: First quadrant of forming limit diagram for Marciniak-Kuczyńsky test with stochastic distribution of defects (12 distributions for each loading path) with cross-hardening (cross) as well as without cross-hardening plasticity model (non-cross). The markers (black circles and red squares) show the obtained single values on the forming limit diagram curve in the different stochastic simulations. The scattering is increasing from plane strain tension to equibiaxial stretching for both model responses where the direction of the scattering is related to the loading path only. The mean curve represents the average of all stochastic simulations. For a stochastic distribution a critical amount of local localization has to be present in one cell before these are recognized globally as formability limit. The simulated strains of the forming limit diagram are compared with experimental results for IF tailor welded blanks from [33] indicating that the numerical results are at the correct order of formability of such steels. (For interpretation of the references to color in this figure legend, the reader is referred to the web version of this article.)

loading conditions reaching from a equibiaxial stretching to a uniaxial tensile loading are achievable.

The full simulation set-up is illustrated in Fig. 11b). The contact conditions play a crucial role in the Nakazima test. Coulomb friction with a friction coefficient $\mu = 0.1$ is assumed between blank and die as well as blank and blank holder where the contact between punch and blank is modeled frictionless to minimize the influence on the formability prediction. The sliding motion of the sheet is prevented using a draw-bead which is located at $R = 66$ mm and which has a radius of $r_d = 1.5$ mm. The simulation consists of two consecutive steps. First, the blank is clamped by pressing the blank holder against the die. Afterwards, the punch moves at a constant velocity perpendicular to the blank plane. The investigated specimen geometries with its mesh discretizations are illustrated in Fig. 12. The specimen with $r = 0$ mm represents a equibiaxial loading case where for $r = 85$ mm a uniaxial tensile loading is achieved. Since uniformity of the emerging fields is not the case, there is no need for an additional localization triggering mechanism, hence material parameters are assumed to be uniformly distributed. Thus, no additional defects are present in the metal sheet.

Fig. 13 exemplary shows the distribution of equivalent plastic strain after strain localization occurred in the different investigated specimens. The different loading cases are clearly captured by the localization patterns. As expected, the reduction of material and more uniaxial loading leads to an earlier localization phenomena at the center region of the specimen.

To analyze the behavior of the different specimens and material models (cross-hardening vs. non-cross-hardening model) quantitatively, Fig. 14 displays the punch force over the punch dis-

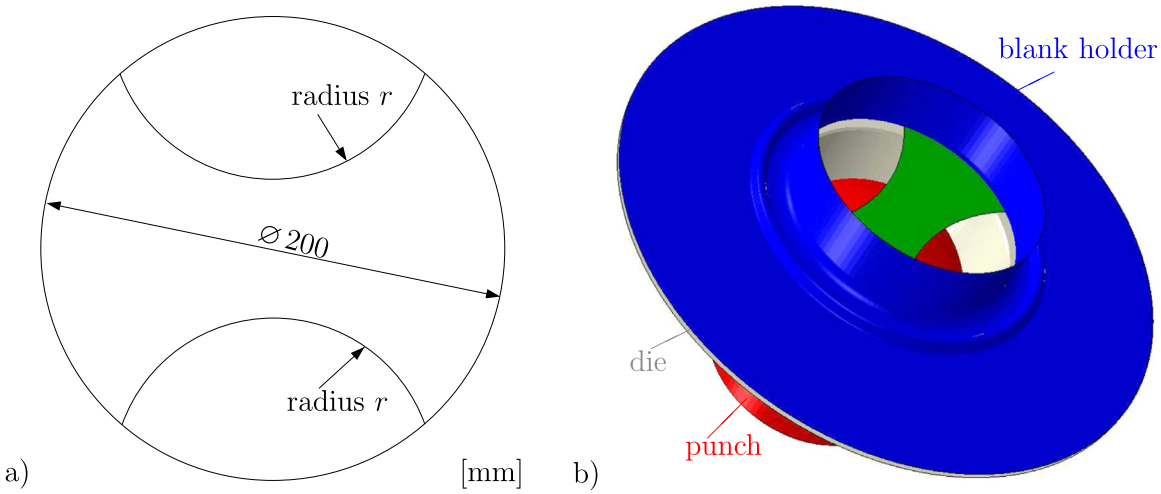

Fig. 11. Nakazima test simulations: a) Geometry of the sheet. From the circular blank, radii of different radius r are cut out. Different radii are used to achieve different stress states. b) Complete simulation set-up of Nakazima Test, involving hemispherical punch, blank holder and die. The contact between punch and blank is assumed to be as frictionless where the contact between blank and die as well as blank holder is modeled via Coulomb friction with a friction coefficient $\mu = 0.1$. In a first step, the blank holder is pressed against the die to clamp the blank between die and blank holder. In the next step, the punch moves perpendicular to the blank plane at a constant velocity.

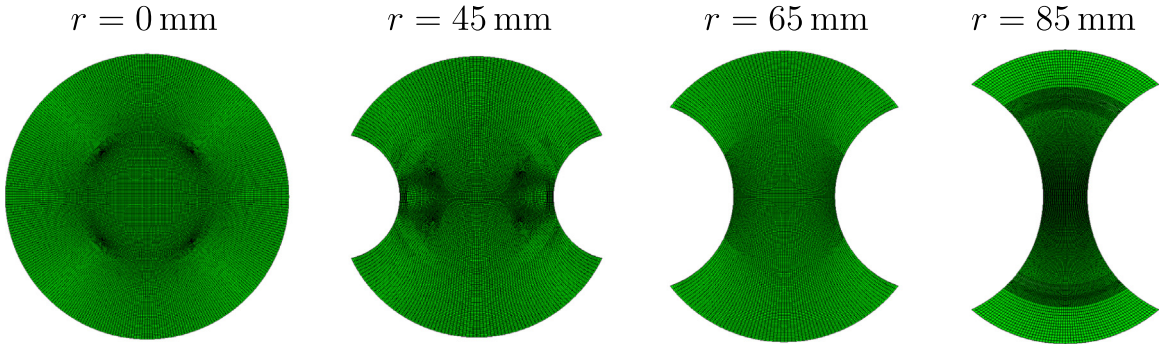

Fig. 12. Nakazima test simulations: Mesh discretization of sheets with different cut geometries used in the Nakazima test simulations. The full blank represents equibiaxial loading case where the most waisted blank is representative for simple tensile loading.

placement of the different simulation cases. Strain localization goes along with the decrease of the required punch force in loading direction. The punch force increases with decreasing cutting radius r as well as localization occurs at a larger displacement. The difference between both material models is significant for smaller cutting radii where the cross-hardening model predicts a significant improved formability. For $r = 85$ mm no difference is notable which perfectly fits with the theoretical expectation. As seen already from the Marciniak-Kuczyńsky results (see Fig. 10), for plane strain loading no deviation between both material models is notable as the yield curvature is the same for this point of loading (see results in Soyarslan et al. [34] as well). The case of uniaxial tension is located in the second quadrant of the forming limit diagram for which both models are predicting identical values as cross-hardening is only relevant for loading paths orthogonal to the primary loading direction due to the evolving dislocation structure perpendicular to the loading (latent hardening). As the biaxiality of the loading increases the difference in the formability predictions increases which is visible in the Nakazima test simulations as well.

6. Conclusion

In this paper we investigate the role of reduction in the yield locus curvature associated with cross hardening on the shape of the forming limit diagrams in the first quadrant. For this purpose, Levkovitch-Svendsen's cross-hardening model is used [22] with an assumption of initial material isotropy. A reduced plane-stress formulation is developed and implemented as a user defined material subroutine into Abaqus. The implementation is verified for finite-strain normal and small-strain shear loading scenarios for which analytical derivations are presented. The formability analyses use finite element models of the stochastic Marciniak-Kuczyński and Nakazima tests. As anticipated, decrease of the yield locus curvature with cross hardening relative to the classical J_2 flow theory results in an enhanced formability of the material. More specifically, observed major and minor strains at localization in the Marciniak-Kuczyński tests are higher in the first quadrant except for the plane strain path where there is no path change on the course of localization. For the Nakazima tests, recorded punch displacements at maximum recorded punch forces, which could be identified as the point of localization, are higher with cross

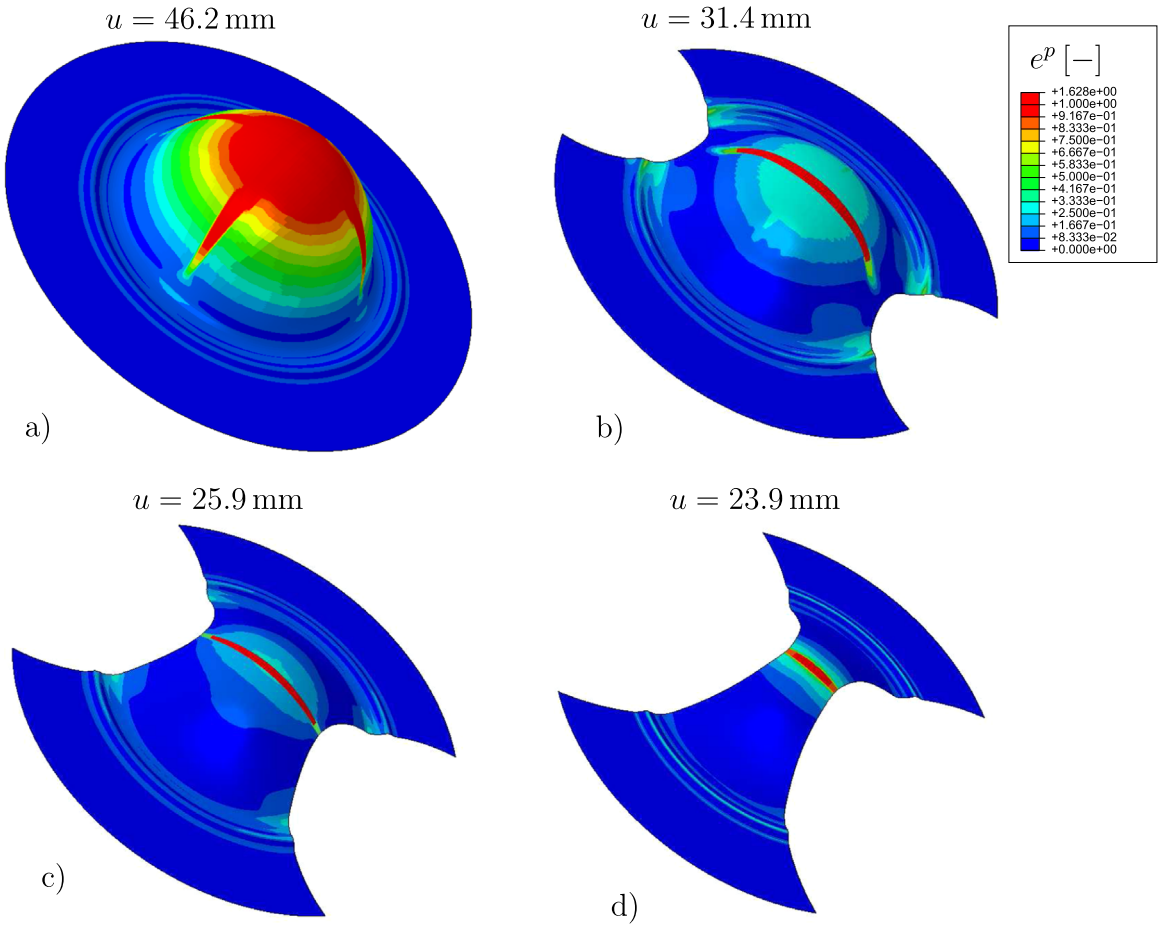

Fig. 13. Nakazima test simulations: Distribution of equivalent plastic strain for sheets with different cut geometries. The distribution of the plastic strain e^p shows the fully developed localization patterns which form depending on the stress stage/loading path invoked by the cut geometries. A more uniaxial loading stage (d) results in an earlier localization. The force drop in the simulation, indicating the formability capabilities, is observed at an earlier displacement.

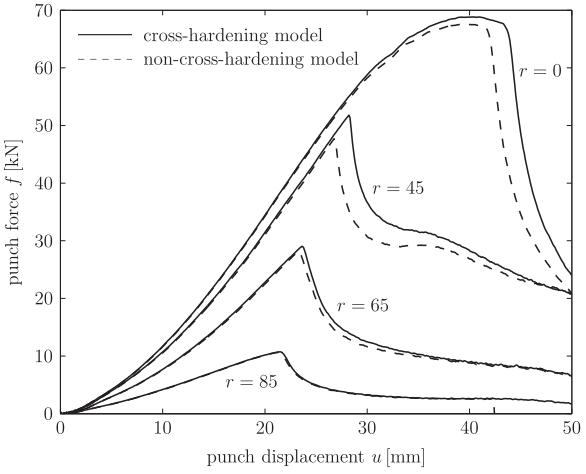

Fig. 14. Nakazima test simulations: Punch force f vs. punch displacement u for four different cut geometries with radii r where r values are given in mm (see Fig. 12). The force and displacement are only representing the component in vertical direction, perpendicular to the plane of the sheet. The force drop indicates the start of localization and the corresponding strain represents the formability limit. For uniaxial tensile loading, both material models predict the same behavior, as cross-hardening is not influencing yield surface curvature in this loading direction.

hardening plasticity as compared to J_2 flow theory. This strongly hints towards a significant increase of formability for cross hardening steel sheets in process chains.

Acknowledgements

Financial support for this work provided by the German Science Foundation (DFG) under contract PAK 250 (TP4) is gratefully acknowledged.

Appendix A. Voigt and Mandel vector notations – a comparison

In a previous work of the authors, the Voigt notation was introduced in formulation of the framework [5]. Voigt notation vectorizes strain-like and stress-like tensors differently. Vector forms of strain-like tensors use the stencil $\left[1\,|\,2\right]^{\mathrm{T}}$ whereas for stress-like tensors the stencil $\left[1\,|\,1\right]^{\mathrm{T}}$ is used. Relating strain-like and stress-like vectors, as in the case of Armstrong-Frederick-type rate form, then requires a transformation operator $\boldsymbol{Q}$ which for the case of 3D reads

$$\boldsymbol{Q} = \frac{1}{2}\begin{bmatrix} 2 & 0 & 0 & 0 & 0 & 0 \\ & 2 & 0 & 0 & 0 & 0 \\ & & 2 & 0 & 0 & 0 \\ & & & 1 & 0 & 0 \\ & & & & 1 & 0 \\ \text{sym.} & & & & & 1 \end{bmatrix}. \tag{A1}$$

Similar to vectors, the matrix forms of the fourth-order tensors used in the quadratic forms $\boldsymbol{x}$: $\boldsymbol{C}$: $\boldsymbol{x}$ differ. If $\boldsymbol{x}$ is of type strain, the

matrix form of $\mathcal{C}$ uses the stencil $\left[\begin{array}{c|c} 1 & 1 \\ \hline 1 & 1 \end{array}\right]$. Otherwise $\left[\begin{array}{c|c} 1 & 2 \\ \hline 2 & 4 \end{array}\right]$ is used.

In this work the Mandel notation is utilized since it allows a more elegant and transparent scheme through a unique mapping in between vector and tensor forms. The most important point is that one does not have to distinguish in between the strain-like and stress-like variables since in the current formulation both uses the stencil $\left[1 \mid \sqrt{2}\right]^{\mathsf{T}}$. This is especially important where rates of strain-like variables are functions of stress-like variables, e.g., as in the case of the Armstrong-Frederic evolution equation for the kinematic hardening strain-like variable. Coming to the matrix notation for fourth-order tensors one has to use a single stencil $\left[\begin{array}{c|c} 1 & \sqrt{2} \\ \hline \sqrt{2} & 2 \end{array}\right]$. This gives a direct consequence where the current notation does not require additional operators such as $\boldsymbol{Q}$.

Appendix B. Extension to finite strains

Let $\boldsymbol{X}$ and $\boldsymbol{x}:=\boldsymbol{\varphi}(\boldsymbol{X}, t)$ denote the particle positions at the reference (undeformed) configuration Ω_0 and current (deformed) configuration Ω respectively. $\boldsymbol{F}:=\partial_{\boldsymbol{X}}\boldsymbol{\varphi}(\boldsymbol{X}, t)$ defines the deformation gradient of the nonlinear map $\boldsymbol{\varphi}$: $\Omega_0 \times \mathbb{R} \to \mathbb{R}^3$ with $\det\boldsymbol{F} > 0$. Any infinitesimal material vector $d\boldsymbol{X}$ at the reference configuration is transformed to its final setting $d\boldsymbol{x}$ at the current configuration via $d\boldsymbol{x}:=\boldsymbol{F}\cdot d\boldsymbol{X}$. Let $\boldsymbol{l}:=\dot{\boldsymbol{F}}\cdot\boldsymbol{F}^{-1} = \partial_{\boldsymbol{x}}\boldsymbol{v}$ denote the spatial velocity gradient with $\boldsymbol{v} = \dot{\boldsymbol{x}}$. The symmetric part of $\boldsymbol{l}$ gives the spatial rate of deformation tensor $\boldsymbol{d}:=\mathrm{sym}(\boldsymbol{l})$. We assume the following rate additive split

$$\boldsymbol{d} = \boldsymbol{d}^e + \boldsymbol{d}^p\,, \tag{B1}$$

with $\boldsymbol{d}^e:=\mathrm{sym}(\boldsymbol{l}^e)$, $\boldsymbol{d}^p:=\mathrm{sym}(\boldsymbol{l}^p)$. This forms the basis of hypoelastic-plastic formulations which rely on certain objective rates of the selected stress measures. Abaqus/Vumat convention uses the Green–Naghdi–McInnis rate of the Cauchy (true) stress $\boldsymbol{\sigma}$ which requires the rotationally neutralized rate of deformation tensor $\dot{\boldsymbol{\varepsilon}}$ which is defined as

$$\dot{\boldsymbol{\varepsilon}} = \boldsymbol{R}^{\mathsf{T}}\cdot\left[\boldsymbol{d}^e + \boldsymbol{d}^p\right]\cdot\boldsymbol{R} = \dot{\boldsymbol{\varepsilon}}^e + \dot{\boldsymbol{\varepsilon}}^p, \tag{B2}$$

with $\dot{\boldsymbol{\varepsilon}}^e:=\boldsymbol{R}^{\mathsf{T}}\cdot\boldsymbol{d}^e\cdot\boldsymbol{R}$, $\dot{\boldsymbol{\varepsilon}}^p:=\boldsymbol{R}^{\mathsf{T}}\cdot\boldsymbol{d}^p\cdot\boldsymbol{R}$. Here, $\boldsymbol{R}$ denotes the rotation tensor, carried out by the polar decomposition of the deformation gradient, $\boldsymbol{F}:=\boldsymbol{R}\cdot\boldsymbol{U}$, with $\boldsymbol{U}$ representing the symmetric right stretch tensor. Similarly, a pull back operation on the Cauchy (true) stress tensor $\boldsymbol{\sigma}$ with the rotation tensor gives its rotationally neutralized counterpart viz $\tilde{\boldsymbol{\sigma}}:=\boldsymbol{R}^{\mathsf{T}}\cdot\boldsymbol{\sigma}\cdot\boldsymbol{R}$ whose material time derivative $\mathring{\tilde{\boldsymbol{\sigma}}}$ can be objectively integrated. Hence, the finite strain extension of the presented framework is realized using the replacements $\dot{\boldsymbol{\sigma}} \rightsquigarrow \mathring{\tilde{\boldsymbol{\sigma}}}$ and $\dot{\boldsymbol{\varepsilon}} \rightsquigarrow \dot{\tilde{\boldsymbol{\varepsilon}}}$ and representing the expressions at the rotationally neutralized configuration.

Appendix C. Correlated random field generation

In development of the correlated random fields, we use the method of circular embedding closely following the work of Kroese and Botev [20] and adapt the Matlab code listed therein. For the sake of completeness, we summarize the method in the following. For further details, the reader is referred to the work of [20] and the references therein. A random field is a spatial stochastic process which consists of a collection of random variables $\{X_{\boldsymbol{r}},\ \boldsymbol{r} \in D\}$ where $D \subset \mathbb{R}^d$ represents a d-dimensional domain and $X_{\boldsymbol{r}}$ is a random quantity associated with a spatial position $\boldsymbol{r}$. In the current case we are only interested in 2-dimensional domains, that is $D \subset \mathbb{R}^2$. The set of possible values of $X_{\boldsymbol{r}}$ is called the state space of the spatial process. We are considering a discrete number of material points in the domain which are assigned a continuous material property, hence this stands for a process with a discrete index set and a continuous state space. We assume that the random field $\{\overline{X}_{\boldsymbol{r}},\ \boldsymbol{r} \in \mathbb{R}^2\}$ is Gaussian such that the multivariate normal vector $\boldsymbol{X}$ has the property $\boldsymbol{X} = [\overline{X}_1, \overline{X}_2, \ldots, \overline{X}_n]^{\mathsf{T}} = [\overline{X}_{\boldsymbol{r}_1}, \overline{X}_{\boldsymbol{r}_2}, \ldots, \overline{X}_{\boldsymbol{r}_n}]^{\mathsf{T}} \sim \mathcal{N}(\boldsymbol{\mu}, \boldsymbol{\Sigma})$ where $\boldsymbol{\mu}$ and $\boldsymbol{\Sigma}$ denote expectation vector and covariance matrix, respectively. The Gaussian random field is determined completely by its expectation function $\widetilde{\boldsymbol{\mu}}_{\boldsymbol{r}} = \mathbb{E}\overline{X}_{\boldsymbol{r}}$ and covariance function $\widetilde{\boldsymbol{\Sigma}}_{\boldsymbol{r},\boldsymbol{s}} = \mathrm{Cov}(\overline{X}_{\boldsymbol{r}}, \overline{X}_{\boldsymbol{s}})$ with $\boldsymbol{r}, \boldsymbol{s} \in D$. With the stationarity of the Gaussian process, we have a constant $\mathbb{E}\overline{X}_{\boldsymbol{r}}$ and invariant $\mathrm{Cov}(\overline{X}_{\boldsymbol{r}}, \overline{X}_{\boldsymbol{s}})$ under translations, with $\mathrm{Cov}(\overline{X}_{\boldsymbol{r}+\boldsymbol{d}}, \overline{X}_{\boldsymbol{s}+\boldsymbol{d}}) = \mathrm{Cov}(\overline{X}_{\boldsymbol{r}}, \overline{X}_{\boldsymbol{s}})$ for an arbitrary vector $\boldsymbol{d}$.

We wish to generate a zero-mean stationary Gaussian random field $\{\overline{X}_{\boldsymbol{r}}\}$ on each of the grid points $\{(i, j)/n, i = 0, 1, \ldots, n-1, j = 0, 1, \ldots, n-1\}$ corresponding to a Gaussian covariance function of the form

$$\mathrm{Cov}\left(\overline{X}_{\boldsymbol{r}}, \overline{X}_{\boldsymbol{s}}\right) = \phi\left(\boldsymbol{r} - \boldsymbol{s}\right) = \exp\left(\frac{-|\boldsymbol{r} - \boldsymbol{s}|^2}{L_c^2}\right), \tag{C1}$$

where $|\boldsymbol{r} - \boldsymbol{s}|^2 = [r_1 - s_1]^2 + [r_2 - s_2]^2$ and L_c corresponds to the correlation length. Thus, the process is also isotropic, i.e. it does not depend on the selected orientation. Over the grid, the values of the Gaussian process are gathered in an $n^2 \times 1$ column vector $\boldsymbol{X}$. The covariance matrix $\Omega_{ij} = \phi(\boldsymbol{r}_i - \boldsymbol{s}_j)$, $i, j = 1, 2, \ldots n^2$ has a symmetric block-Toeplitz[3] structure and $\boldsymbol{\Omega}$ is uniquely characterized by its first block row $[\boldsymbol{R}_1, \boldsymbol{R}_2, \ldots, \boldsymbol{R}_n]$ where each block is an $n \times n$ Toeplitz matrix, which is not necessarily symmetric. Each $\boldsymbol{R}_k$ is embedded in the upper left corner of the circulant matrix $\boldsymbol{C}_k$. The entries of the first block row $[\boldsymbol{C}_1, \boldsymbol{C}_2, \ldots, \boldsymbol{C}_n, \boldsymbol{C}_n^{\mathsf{T}}, \boldsymbol{C}_{n-1}^{\mathsf{T}}, \ldots, \boldsymbol{C}_2^{\mathsf{T}}]$ of the $[2n-1]^2 \times [2n-1]^2$ block circulant matrix $\boldsymbol{\Sigma}$ are stored in a $[2n-1] \times [2n-1]$ matrix $\boldsymbol{G}$.

After completing the embedding in block circulant matrix we diagonalize it with $\boldsymbol{\Sigma} = \boldsymbol{P}^{\star}\cdot\mathrm{diag}(\boldsymbol{\gamma})\cdot\boldsymbol{P}$, where $\boldsymbol{P}$ is the $[2n-1]^2 \times [2n-1]^2$ two-dimensional discrete Fourier transform matrix with $\boldsymbol{P} = \boldsymbol{F} \otimes \boldsymbol{F}$, where $F_{jk} = \exp(2\pi\mathrm{i}jk/n)/\sqrt{n}$ with $j, k = 0, 1, \ldots, n-1$. $[\bullet]^{\star}$ represents the complex conjugate transpose of $[\bullet]$. Ordering the eigenvalue vector $\boldsymbol{\gamma} = [\gamma_1, \gamma_2, \ldots, \gamma_{[2n-1]^2}]$ we reach an $[2n-1] \times [2n-1]$ matrix $\boldsymbol{\Gamma}$ which is the (appropriately scaled) two-dimensional Fast Fourier Transform (FFT2) of $\boldsymbol{G}$. Denoting the component-wise square root operation with $\sqrt{[\bullet]}$, we define the matrix $\boldsymbol{B} = \boldsymbol{P}^{\star}\cdot\mathrm{diag}(\sqrt{\boldsymbol{\gamma}})$ where $\boldsymbol{\Sigma} = \boldsymbol{B}^{\star}\cdot\boldsymbol{B}$.

Finally, letting the components $\underline{Z}_{jk} = U_{jk} + \mathrm{i}\,V_{jk}$ where $U_{jk}, V_{jk} \sim \mathcal{N}(0, 1)$ make up the $[2n-1] \times [2n-1]$ complex Gaussian matrix $\underline{\boldsymbol{Z}}$, we reach realizations of a correlated stationary Gaussian field on the grid through the first $n \times n$ sub-blocks of the real and the imaginary parts of the FFT2 of the array $\sqrt{\boldsymbol{\Gamma}} \odot \underline{\boldsymbol{Z}}$ where $\odot$ represents element by element multiplication.

References

[1] Banabic D. Sheet metal forming processes.Berlin, Heidelberg: Springer-Verlag; 2010.

[2] Barlat F, Gracio JJ, Lee M-G, Rauch EF, Vincze G. An alternative to kinematic hardening in classical plasticity. Int J Plast 2011;27(9):1309–27.

[3] Barlat F, Ha J, Gracio JJ, Lee MG, Rauch EF, Vincze G. Extension of homogeneous anisotropic hardening model to cross-loading with latent effects. Int J Plast 2013;46:130–42.

[4] Barthel C, Klusemann B, Denzer R, Svendsen B. Modeling of a thermo-mechanical process chain for sheet steels. Int J Mech Sci 2013;74:46–54.

[5] Behrouzi A, Soyarslan C, Klusemann B, Bargmann S. Inherent and induced

[3] If its components along each diagonal are the same, an $N \times N$ matrix is referred to as Toeplitz.

anisotropic finite visco-plasticity with applications to the forming of DC06 sheets. Int J Mech Sci 2014;89:101–11.
[6] Clausmeyer T, van den Boogaard H, Noman M, Gershteyn G, Schaper M, Svendsen B, Bargmann S. Phenomenological modeling of anisotropy induced by evolution of the dislocation structure on the macroscopic and microscopic scale. Int J Mater Form 2011;4:141–54.
[7] Feigenbaum HP, Dafalias YF. Directional distortional hardening in metal plasticity within thermodynamics. Int J Solids Struct 2007;44:7526–42.
[8] Ghazanfari A, Assempour A. Calibration of forming limit diagrams using a modified MarciniakKuczyńsky model and an empirical law. Mater Des 2012;34:185–91.
[9] Ghosh A. The influence of strain hardening and strain-rate sensitivity on sheet metal forming. J Eng Mater Technol 1977;99(3):264–74.
[10] Goodwin G. Application of strain analysis to sheet metal forming problems in the press shop. SAE Technical Paper; 1968. p. 680093.
[11] Hill R. A theory of the yielding and plastic flow of anisotropic metals. In: Proceedings of the royal society of London, vol. 193. 1948. p. 281–97.
[12] Hutchinson J, Neale K. Influence of strain-rate sensitivity on necking under uniaxial tension. Acta Metall 1977;25(8):839–46.
[13] Hutchinson JW, Neale KW. Mechanics of sheet metal forming: material behavior and deformation analysis. Springer US, Boston, MA, Ch. Sheet Necking-III. Strain-Rate Effects; 1978. p. 269–285.
[14] Inal K, Neale K, Aboutajeddine A. Forming limit comparisons for {FCC} and {BCC}sheets. Int J Plast 2005;21(6):1255–66.
[15] Johnson G, Cook W. A constitutive model and data for metals subjected to large strains, high strain rates and high temperatures. In: Proceedings of the 7th international symposium on ballistics, The Hague; 1983. p. 541–7.
[16] Keeler S, Backofen W. Plastic instability and fracture in sheets stretched over rigid punches. Trans Am Soc Met 1963;56:25–48.
[17] Khan AS, Baig M. Anisotropic responses, constitutive modeling and the effects of strain-rate and temperature on the formability of an aluminum alloy. Int J Plast 2011;27(4):522–38.
[18] Kim JH, Lee M-G, Kim D, Barlat F. Numerical procedures for predicting localization in sheet metals using crystal plasticity. Comput Mater Sci 2013;72:107–15.
[19] Kim D, Kim H, Kim JH, Lee M-G, Kim KJ, Barlat F, Lee Y, Chung K. Modeling of forming limit for multilayer sheets based on strain-rate potentials. Int J Plast 2015;75:63–99.
[20] Kroese DP, Botev ZI. Spatial process generation, arXiv:1308.0399.
[21] Lee M-G, Kim D, Kim C, Wenner M, Wagoner R, Chung K. A practical two-surface plasticity model and its application to spring-back prediction. Int J Plast 2007;23(7):1189–212.
[22] Levkovitch V, Svendsen B. Accurate hardening modeling as basis for the realistic simulation of sheet forming processes with complex strain-path change, In: J Cesar de Sa (Edition), 9th International Conference on Numerical Methods in Industrial Forming Processes (NUMIFORM 2007), Porto, Portugal, vol. 2. AIP Conference Proceedings; 2007. p. 1331–36.
[23] Lu XZ, Chan LC. Numerical simulation for thermal and rt forming light sheet materials using a new combined model of m-k theory and shear localization criterion. Int J Adv Manuf Technol 2016;83(1):357–63.
[24] Marciniak Z, Kuczyński K. Limit strains in the processes of stretch-forming sheet metal. Int J Mech Sci 1967;9(9):609–20.
[25] Marciniak Z, Kuczyński K, Pokora T. Influence of the plastic properties of a material on the forming limit diagram for sheet metal in tension. Int J Mech Sci 1973;15(10):789–800.
[26] Min J, Lin J, Li J, Bao W. Investigation on hot forming limits of high strength steel 22MnB5. Comput Mater Sci 2010;49(2):326–32.
[27] Min J, Hector LG, Lin J, Carter JT. Analytical method for forming limit diagram prediction with application to a magnesium ZEK100-O alloy. J Mater Eng Perform 2013;22(11):3324–36.
[28] Nakazima K, Kikuma T, Asuka K. Study on the formability of steel sheet. Yawata Technical Report, No 264; 1968, September.
[29] Narasimhan K, Wagoner RH. Finite element modeling simulation of in-plane forming limit diagrams of sheets containing finite defects. Metal Trans A 1991;22A:2655–65.
[30] Ortiz M, Simo JC. An analysis of a new class of integration algorithms for elastoplastic constitutive relations. Int J Numer Methods Eng 1986;23:353–66.
[31] Pietryga MP, Vladimirov IN, Reese S. A finite deformation model for evolving flow anisotropy with distortional hardening including experimental validation. Mech Mater 2012;44:163–73.
[32] Rabahallah M, Balan T, Bouvier S, Bacroix B, Barlat F, Chung K, Teodosiu C. Parameter identification of advanced plastic strain rate potentials and impact on plastic anisotropy prediction. Int J Plast 2009;25(3):491–512.
[33] Safdarian R. Forming limit diagram prediction of tailor welded blank by modified MK model. Mech Res Commun 2015;67:47–57.
[34] Soyarslan C, Klusemann B, Bargmann S. A directional modification of the Levkovitch-Svendsen cross-hardening model based on the stress deviator. Mech Mater 2015;86:21–30.
[35] Stören S, Rice J. Localized necking in thin sheets. J Mech Phys Solids 1975;23(6):421–41.
[36] Teodosiu C, Hu Z. Evolution of the intragranular microstructure at moderate and large strains: modelling and computational significance. In: Shen S, Dawson P, editors. Simulation of materials processing: theory, methods and applications. Rotterdam: Balkema; 1995. p. 173–82.
[37] Tvergaard V. Effect of kinematic hardening on localized necking in biaxially stretched sheets. Int J Mech Sci 1978;20:651–8.
[38] Wagoner RH, Lim H, Lee M-G. Advanced issues in springback. Int J Plast 2013;45:3–20.
[39] Wagoner RH, Chenot JL. Metal forming analysis.Cambridge: Cambridge University Press; 2001.
[40] Wang W, Sluys L, de Borst R. Viscoplasticity for instabilities due to strain softening and strain-rate softening. Int J Numer Methods Eng 1997;40:3839–64.
[41] Zhang C, Leotoing L, Guines D, Ragneau E. Theoretical and numerical study of strain rate sensitivity on formability of sheet metal. Numisheet 2008:1–5.
[42] Zhang C, Leotoing L, Guines D, Ragneau E. Theoretical and numerical study of strain rate influence on AA5083 formability. J Mater Process Technol 2009;209(8):3849–58.